**Danny Love Wamba Djukem · Xuanmei Fan · Anika Braun ·
Marie-Luce Chevalier · Xin Wang · Lanxin Dai · Chengyong Fang · Xinxin Zhang ·
Tolga Gorum · Qiang Xu · Hans-Balder Havenith**

Traditional and modified Newmark displacement methods after the 2022 M$_s$ 6.8 Luding earthquake (Eastern Tibetan Plateau)

Abstract The Newmark displacement (ND) method, which reproduces the interactions between waves, solids, and fluids during an earthquake, has experienced numerous modifications. We compare the performances of a traditional and a modified version of the ND method through the analysis of co-seismic landslides triggered by the 2022 Ms 6.8 Luding earthquake (Sichuan, China). We implemented 23 ND scenarios with each equation, assuming different landslide depths, as well as various soil-rock geomechanical properties derived from previous studies in regions of similar lithology. These scenarios allowed verifying the presence or absence of such landslides and predict the likely occurrence locations. We evaluated the topographic and slope aspect amplification effects on both equations. The oldest equation has a better landslide predictive ability, as it considers both slope stability and earthquake intensity. Contrarily, the newer version of the ND method has a greater emphasis on slope stability compared to the earthquake intensity and hence tends to give high ND values only when the critical acceleration is weak. The topographic amplification does not improve the predictive capacity of these equations, most likely because few or no massive landslides were triggered from mountain peaks. This approach allows structural, focal mechanism, and site effects to be considered when designing ND models, which could help to explain and predict new landslide distribution patterns such as the abundance of landslides on the NE, E, S, and SE-facing slopes observed in the Luding case.

Keywords Co-seismic landslides · Earthquake intensity · Topographic amplification · Site effects · Slope aspect · Focal mechanism effect

Introduction

Seismic waves propagate through several layers of soil and rocks before reaching the surface. The intensity of ground motion observed at the Earth's surface is determined by earthquake magnitude, distance from the source, ground motion parameters, and site effects (Gazetas 1982; Kramer 1996; Akkar et al. 2014; Anderson 2003; Kawase 2003; Kubo et al. 2020). Earthquakes often cause significant damages through a series of cascading effects, including landslides (Yin et al. 2009; Bertrand et al. 2011; Zêzere et al. 2017; Cetin et al. 2022; Shinohara and Kume 2022). The term "landslide" defines the movement of a mass of rock, debris, or soil, down a slope when the shear stress exceeds the shear strength of the material (Cruden and Varnes 1996; Van Westen et al. 2006).

The 5 September 2022 Ms 6.8 Luding earthquake created a surface deformation of about 35 km, although co-seismic earthquake surface ruptures were only a few tens of meters long (en-echelon cracks), mostly destroyed by the numerous landslides (Li Haibing's personal communication, Institute of Geology, Chinese Academy of Geological Sciences, 100,037 Beijing, China). This earthquake triggered catastrophic secondary effects ranging from landslides and rockfalls to collapses. The latter resulted in approximately 93 deaths, 25 missing persons, and the destruction of more than 50,000 houses.

The purely statistical assessment of landslides triggered by earthquakes has been investigated by Lombardo and Tanyas (2022); Havenith et al. (2022); He and Xu (2022); and Shao et al. (2022). Physically based methods have also been used, although less often (Jibson 2007; Jibson 2011; Cui et al. 2019; van den Bout et al. 2022; Chen et al. 2023). Furthermore, effective modeling of earthquake-induced landslides requires correct simulation of seismic wave propagation, interaction with the material's geomechanical properties, and pore water pressure, during and after the earthquake (Taiebat et al. 2010; Xue et al. 2013). A geomechanical method named the "Newmark displacement method" (Newmark 1965) has been adapted in an empirical approach by Jibson (1993) and Harp and Jibson (1996) for the spatial analysis of earthquake-triggered landslides. This method qualitatively and quantitatively reproduces (according to available seismological data) the interactions between waves, solids, and (on-site) fluids during an earthquake. The Newmark displacement (hereafter ND) method allows to control the type of contributing process (attenuation with distance or type of fault rupture) and the prediction of future landslide locations.

The ND method initially proposed by Newmark (1965) equated a landslide to a block sliding on an inclined plane. This method remains one of the most used, physics-based, models to simulate co-seismic permanent displacements in terms of failure probability of slopes. It calculates the critical acceleration (A_c) that sufficiently reduces the shear resistance to trigger ground motion, when seismic intensity exceeds the seismic strength of the slope (Jibson et al. 2004, 2006; Jibson 2011; Chen et al. 2019; Jin et al. 2019; Xi et al. 2022). The traditional and modified forms of the ND method have been successfully implemented to evaluate co-seismic landslides triggered by the 1994 M$_w$ 6.7 Northridge, 1999 M$_w$ 7.5 Chi-Chi, 2008 M$_w$ 7.9 Wenchuan, 98 earthquakes in Greece, 2013 M$_s$ 7.0 Lushan, Kumaun Himalaya, 2015 M$_w$ 7.8 Gorkha, and Mid Niigata Prefecture earthquakes (e.g., Jibson et al. 2000; Wang and

Lin 2010; Chen et al. 2014; Chousianitis et al. 2014; Yuan et al. 2016; Shinoda and Miyata 2017; Jin et al. 2019; Kumar et al. 2021; Maharjan et al. 2021).

However, the traditional Newmark equation has high uncertainties (Jin et al. 2018), is not suitable for all regions, and tends to underestimate the real displacement value. In addition, this equation does not consider the attenuation effect caused by the shear strength on the sliding surface (Jin et al. 2019). Numerous scientists (Wilson and Keefer 1983; Miles and Ho 1999; Jibson 1993, 2007; Jibson et al. 1998, 2000; Chousianitis et al. 2014; Jin et al. 2018) have attempted to modify the traditional formula, mainly by changing the coefficients. New equation members have also been introduced for several laws. Attenuation coefficients were added to the effective internal friction angle and effective cohesion by Jin et al. (2019). Zang et al. (2020) added roughness and potential landslide size. These modifications are believed to have increased the predictive power of the ND method and its universality. However, many uncertainties might also have been introduced, as in the case of Jin et al.'s (2018) equation, hereafter called J18.

Few studies currently compare the predictive power of these new equations with the old ones. Here, we implement two versions of the ND equations to analyze co-seismic landslides triggered by the 5 September 2022 M_s 6.8 Luding earthquake. The first equation is one of the oldest proposed by Miles and Ho (1999) or M99. The second is one of the most recent modified versions with a higher regression coefficient, proposed by J18, where they applied this equation to the analysis of landslides triggered by the 2008 Wenchuan and 2013 Lushan earthquakes. They concluded that this new equation was better suited for the co-seismic landslides' prediction in southwest China; although, they do not consider the various tectonic settings in which an earthquake occurs, i.e., either compressional, extensional, or strike-slip. However, the accuracy of the J18 equation has not yet been examined in another region of southwestern China, where our study area is located.

Moreover, the seismic wave propagation effect, which represents the complete path of the seismic waves between the source and the receiver, is strongly influenced by site effects, which reflect the changes in the overall path of the waves between the epicenter and the immediate location of the site. Site effects depend on lithology, local topography, geomorphology (valleys or basins), and the water table (Geli et al. 1988; Athanasopoulos et al. 1999; Havenith et al. 2002; Assimaki et al. 2005; Biondi and Maugeri 2005; Falcone et al. 2018; di Lernia et al. 2023). These site effects should be considered when characterizing seismic slope movements, as they may amplify or reduce seismic movements as they approach the ground surface. We therefore compare a traditional (M99) and an improved version (J18) of the ND method, integrating the effect of topography and slope orientation on earthquake amplification. This provides a good opportunity to validate whether the modifications made over several decades really yielded more accurate equations, applicable in regions other than those from which they originated.

Study area's background

The study area (Fig. 1A, B) is located along the eastern margin of the Tibetan Plateau. The climate is temperate with heavy rainfall (> 900 mm/yr) in places, from the Indian summer monsoon entering SE Tibet from the deeply incised river valleys (Bookhagen and Burbank 2010; Yu et al. 2022). This area is located between latitudes

29°20′N and 29°40′N and longitudes 102°0′E and 102°15′E, covering ~ 7300 km². Elevation ranges between 830 and 7556 m a.s.l. (Gongga Shan, the highest peak in eastern Tibet).

The 2022 M_s 6.8 Luding earthquake occurred along the Moxi fault, a single and linear segment of the SE Xianshuihe fault (XSHF), along which one earthquake of M > 6.5 occurs on average every 35 years (Xu et al. 2015; Chang et al. 2016; Bai et al. 2021). The trace of this fault has been simplified to a linear line (dark red) for the design of our models, but the real trace is shown in bright red in Fig. 1C. The ~ 1400 km-long left-lateral strike-slip Xianshuihe fault system (XFS) extends from central Tibet to Kunming and the Red River region. This fault system consists of several NW-striking segments such as the Yushu/Batang, Ganzi, Xianshuihe, and Anninghe-Zemuhe-Xiaojiang faults (e.g., Allen et al. 1991). The Xianshuihe fault offsets by ~ 60 km (e.g., Yan and Lin 2015), the Longmenshan thrust belt, along which the 2008 M_w 7.9 earthquake occurred, which triggered countless of large landslides (Chigira et al. 2010). The Xianshuihe fault's late Quaternary slip rate increases from NW (Ganzi fault) to SE (Moxi), from ~ 7 to ~ 13 mm/yr (Chevalier et al. 2018; Bai et al. 2018, 2021), consistent with GNSS studies (Wang and Shen 2020). The 2022 Luding earthquake is the strongest earthquake that occurred in Sichuan province since the 2017 M_s 7.0 Jiuzhaigou earthquake (Yang et al. 2023). The Xianshuihe fault is highly active with at least 29 historical and recorded strong earthquakes of $M \geq 6.5$ since 1725 (Fig. 1B). The last earthquake that occurred along the Moxi segment was in 1786 (M7$^{3/4}$) (Bai et al. 2021 and references therein).

Input data

Here, we present the spatial distribution of landslides triggered by the 2022 Luding earthquake as well as the geoenvironmental factors necessary to compute ND scenarios. The ND computation requires the acceleration time history by integrating twice the values larger than the critical acceleration (A_c) required for inducing sliding. It is computed using A_c, based on the assumptions of the infinite slope model (Ward et al. 1982) and the Arias intensity (I_A) proposed by Keefer et al. (1989). The I_A is considered a quantitative measure of the degree of shaking of an earthquake.

Landslide catalogue

The M_s 6.8 Luding earthquake triggered about 5007 to 5336 landslides as reported by Dai et al. (2023) and Xiao et al. (2023), respectively. The landslide inventory used for this investigation was provided by Dai et al. (2023). They revealed preferred landslide locations on ESE to SSE-oriented slopes corresponding to slope directions varying from 90–135° to 135–180°. Such distribution of landslides versus slope aspect will be discussed later.

Damages are concentrated around the epicenter, especially important west of Moxi town, in the valley leading to Hailuogou national park and glacier (Fig. 2). Landslide surfaces are symbolized by both the black color, which represents the scarps or detachment areas, and the red color, which represents the landslide bodies.

Landslide scarps were automatically extracted from the actual landslide bodies in QGIS 3.18 as the upper 40% of the total area of each landslide polygon from the top. They represent summit zones where landslides are triggered. We tested different
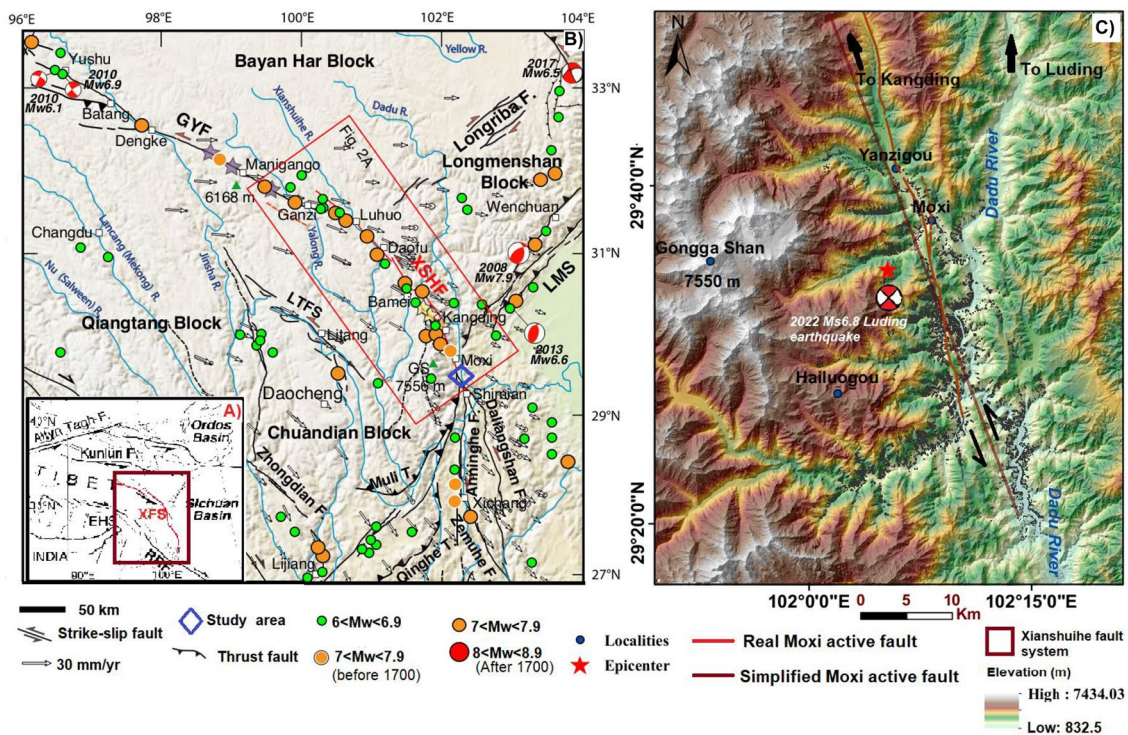
Fig. 1 Overview of the study area: **A** Location of the study area in the eastern Tibetan Plateau with the Xianshuihe fault system (XFS) in red. RRF, Red River fault; EHS, Eastern Himalayan Syntaxis; **B** Seismotectonic map of the Xianshuihe fault (XSHF from Ganzi to Moxi, in red) and Longmenshan fault system (LMS) with digital elevation model in background (modified from Bai et al. 2021). GYF, Ganzi-Yushu fault; LTFS, Litang fault system; GS, Gongga Shan. GNSS vectors from Wang and Shen (2020). **C** Epicenter and left-lateral strike-slip seismogenic Moxi fault segment of the Xianshuihe fault, which triggered the 5 September 2022 Ms 6.8 Luding earthquake; epicenters and focal mechanisms of historical earthquakes of Mw > 6 earthquakes, from 1976 to 2020, including the 2008 Wenchuan, 2010 Yushu, 2013 Lushan, and 2017 Jiuzhaigou earthquakes, are also represented

percentages and found that 40% did not make all the small landslide polygons disappear and allowed for more realistic scarp areas for bigger landslides.

Geoenvironmental and seismic factors necessary to compute ND scenarios

The factor maps with 30×30 m cell size necessary to compute ND scenarios included the mean epicentral distance, slope angle, soil-rock geomechanical properties, curvature, slope aspect, and Arias intensity (I_A). All the above except the slope aspect were used to calculate the unamplified and topographically amplified ND scenarios. The slope aspect, which shows both the direction and steepness of a slope, was used to compute ND slope orientation amplified scenarios. The producing methods of these factors' maps are described below, except the slope aspect, which is more elaborated in the "Influence of the preferred spatial distribution of landslides" section to better analyze the preferred spatial distribution of these landslides.

Mean epicentral distance map
The mean epicentral distance map is the combination of epicentral and activated fault segment distance. This map was produced by digitizing the epicenter point from Dai et al. (2023) and the activated fault segment from Li et al. (2022). The combined distances to both

the epicenter and activated fault segment were computed using the Euclidean distance tool of ArcGIS 10.5. Then, the resulting mean epicentral distance map (Fig. 3a) was obtained using the ArcGIS 10.5 raster calculator. The earthquake-triggered landslides are concentrated around the epicenter and the seismogenic fault (Fig. 3a).

Slope map   The slope angle map was derived from the 30 m Copernicus DEM distributed by the European Space Agency Synergy, Sinergise (2021). This DEM was acquired through the TerraSAR-X add-on for Digital Elevation Measurements (TanDEM-X) mission between 2011 and 2015. We used the spatial analyst tool of ArcGIS 10.5. The slope angle values fluctuate between 0 and 78°, as shown in Fig. 3b.

Selection of soil-rock geomechanical properties   The lithological map (Fig. 4) was extracted from the 1:200 000 global lithological map (Hartmann and Moosdorf 2012). Ice and glaciers are present in the northwestern part of the study area. Surface formations consist of unconsolidated sediment, mixed, siliciclastic, and carbonate sedimentary rocks. Basement rocks are composed of metamorphic, acidic plutonic (granite), basic volcanic, basic plutonic, and pyroclastic rocks.

While we do not have direct soil-rock geomechanical data of the Luding area, the data used to implement our scenarios were estimated from the literature on geophysical and geotechnical investigations, as well as ND applications carried out on similar
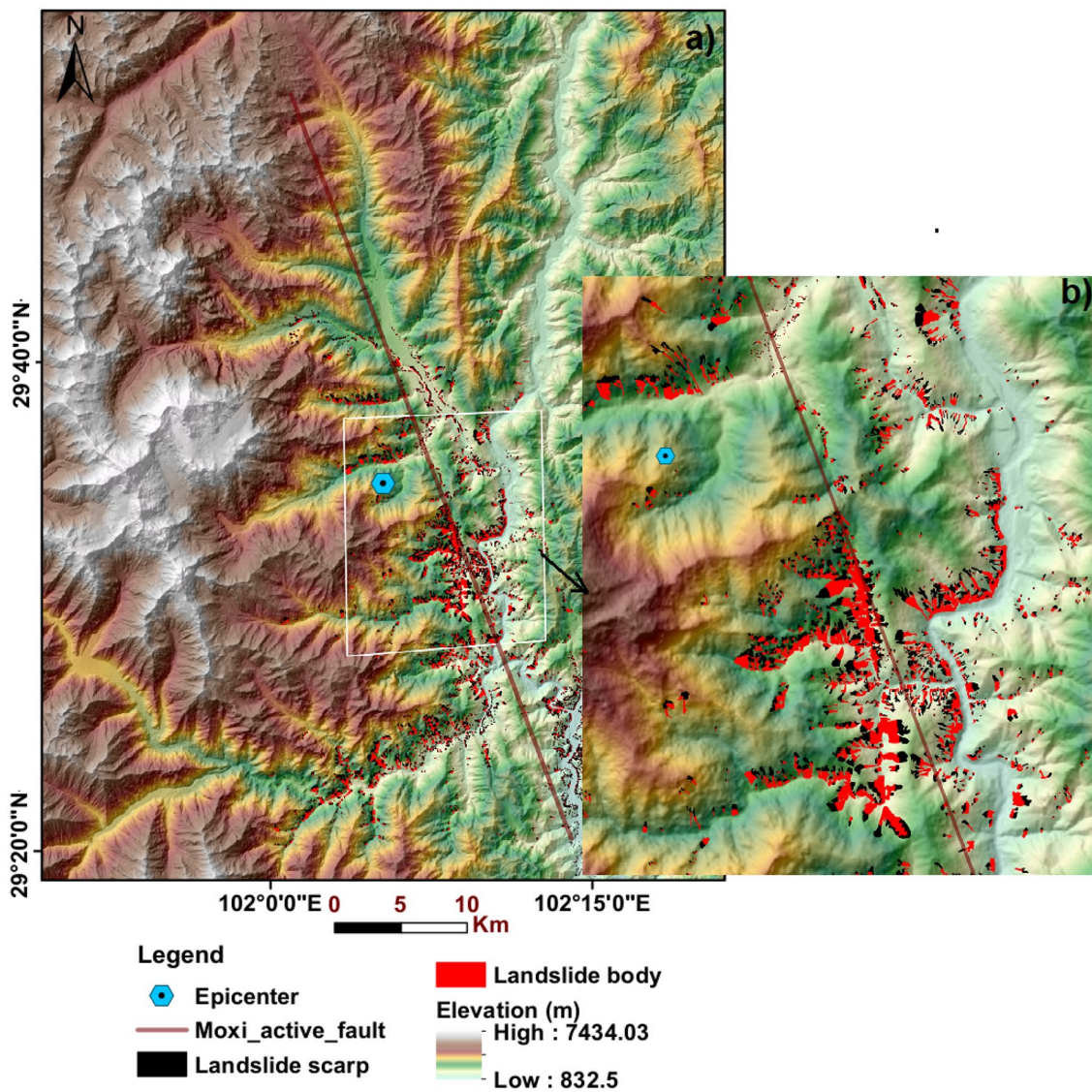
Fig. 2 Spatial distribution of landslide scarps triggered by the Luding earthquake: **a** general view and **b** close-up of the central zone showing landslide scarps in black and landslide bodies in red

rock types. Zang et al. (2020) and Kumar et al. (2021) used these values to analyze co-seismic landslides triggered by the 2014 M_w 6.1 Ludian earthquake in southern China, using the ND approach. The unique values were used over the map and selected values are mostly within the range of these authors' cohesion (c), angle of internal friction (φ), unit weight (γ), and saturation levels (m) values shown in the online Appendix 1 (supplementary material).

Curvature and amplification of the Arias intensity (I_A)   Raster maps used to compute ND scenarios taking into consideration the topographic amplification include those described before, in addition to the amplified curvature and mean epicentral distance. Curvature was derived from the 30 m Copernicus TanDEM-X mission using the spatial analyst tools in ArcGIS 10.5. The curvature values vary between –2 for concave slopes and 2 for convex slopes (Fig. 5a, b). This curvature was derived from the profile and plan curvatures, which

affect the acceleration, deceleration, convergence, and divergence of seismic waves across terrain layers. The curvature is used to determine topographic amplification factors for seismic shaking (Fig. 5b). This amplification was conducted by applying adaptive smoothing operators of 0.8 and 1.5 to the topographic curvature calculated in ArcGIS 10.1 to reproduce the effects of seismic waves on sensitive topographic features (mountain tops and valleys), as proposed by Zevenbergen and Thorne (1987) as well as Moore et al. (1991). Moreover, the maximum topography amplification, varies between 1.6 and 2.0 on the protruded areas, as recommended by Wang et al. (2018). Therefore, the factor 1.5 was used to amplify curvatures ≥ 0.2, 0.8 was used to attenuate the effects of seismic waves on curvatures < − 0.2, and 1 was used for curvatures ≥ 2 and < 2 (Fig. 5d).
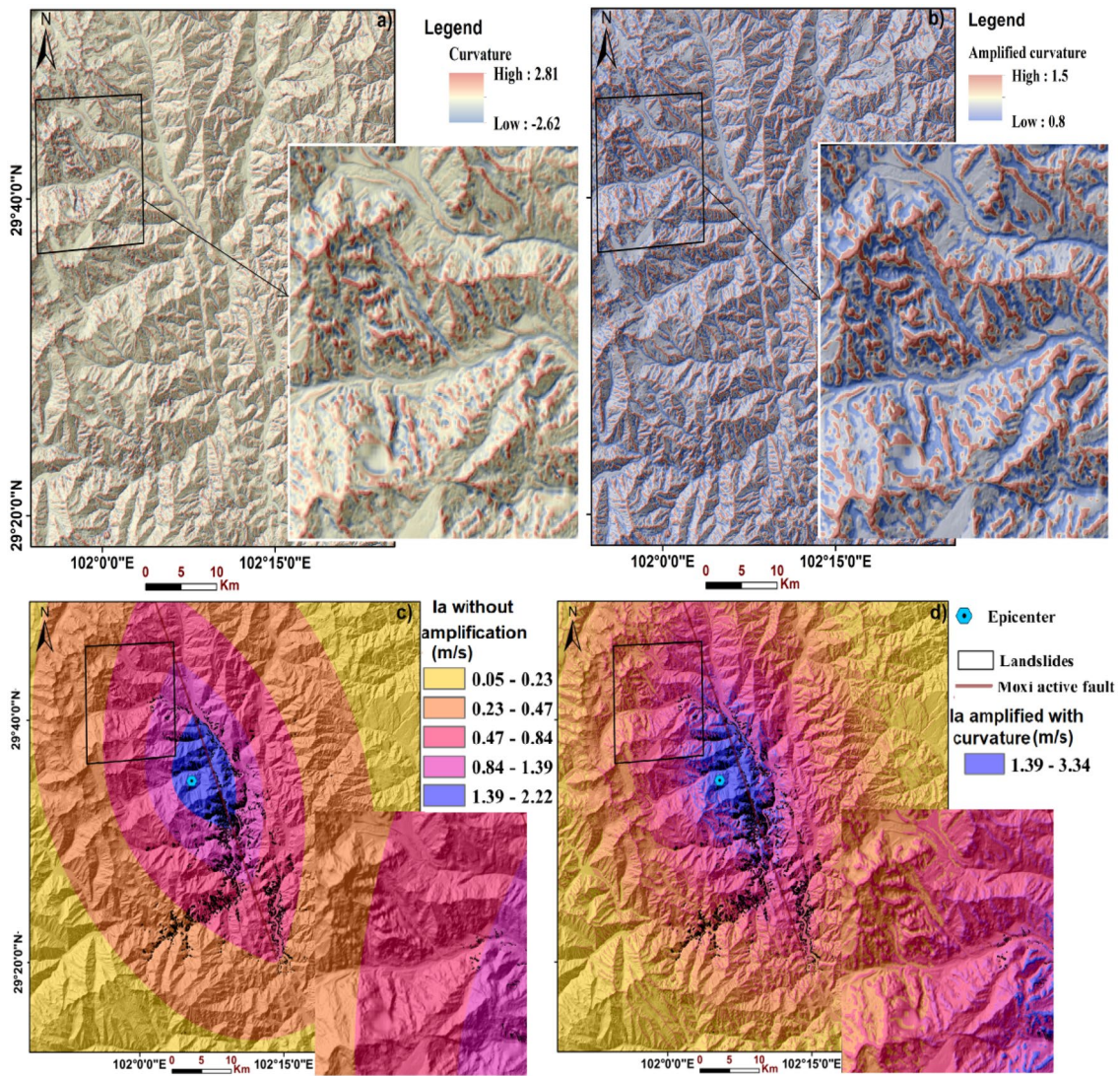
Arias intensity (I_A)   The Arias intensity (Fig. 5c and d) is used to quantify the degree of shaking of an earthquake on a surface (Arias
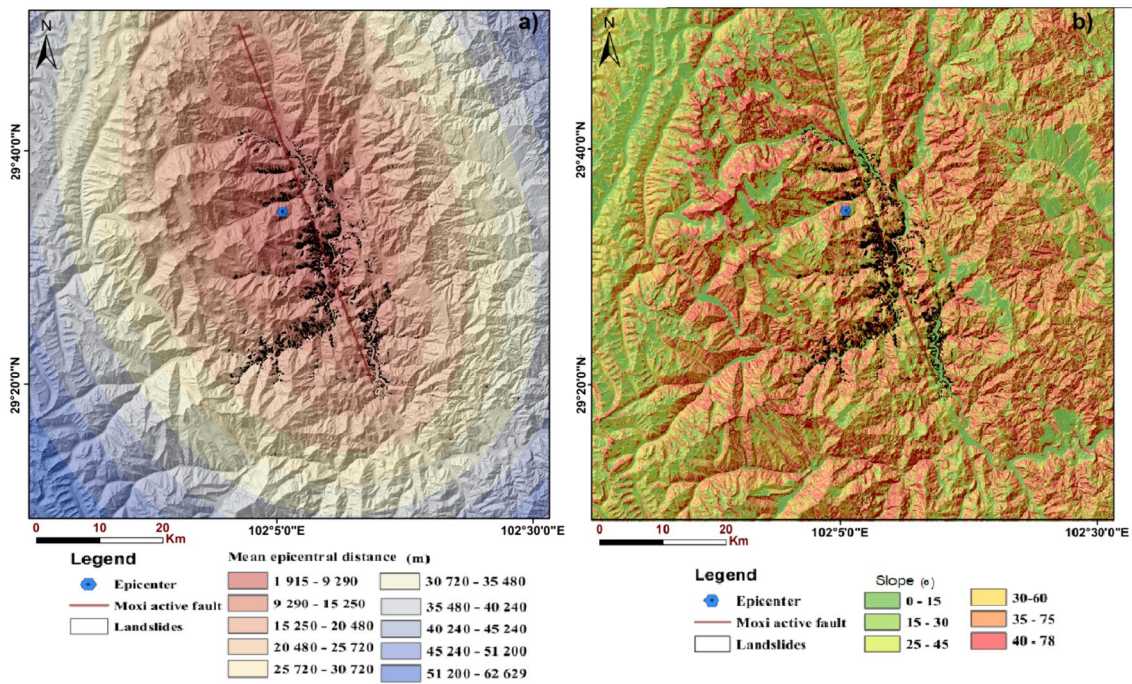
Fig. 3 Geoenvironmental factors: **a** Mean epicentral distance map of the study area. Asymmetric distance distribution as epicenter located on the west side of the fault, where the combined epicentral-fault distances are therefore smaller; **b** Slope map of the study area is subdivided into 6 classes. Landslides are shown by black polygons
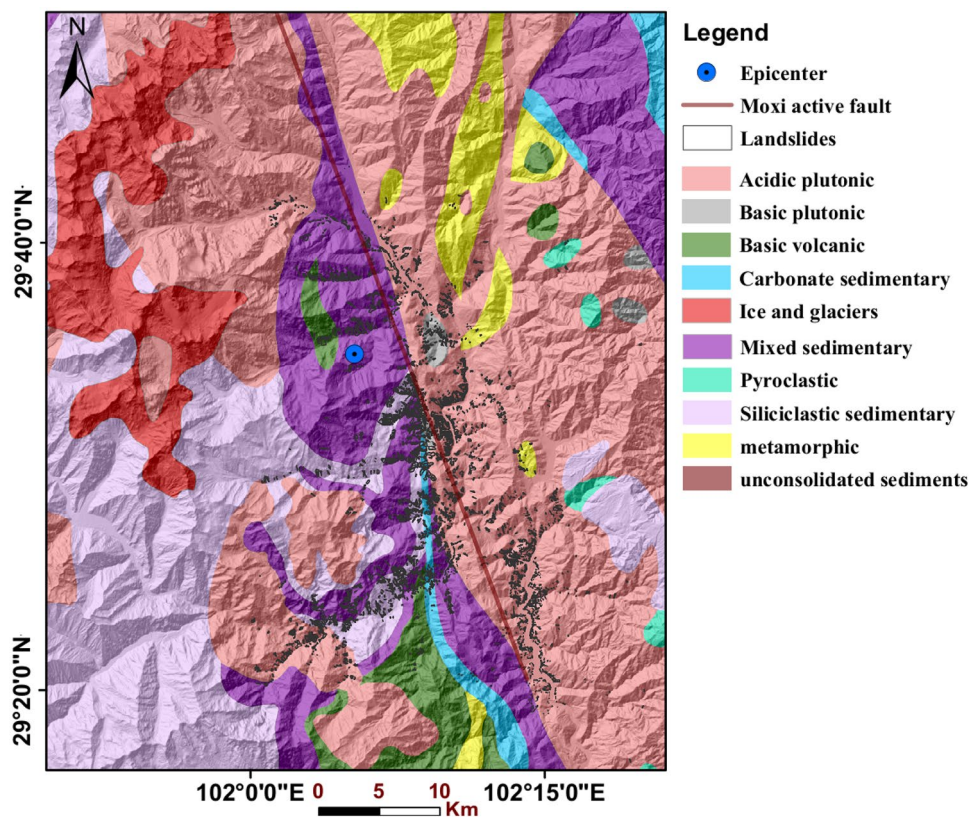
Fig. 4 Lithological map of the Luding area (extracted from Hartmann and Moosdorf 2012)

Fig. 5 **a** Curvature maps of the Luding earthquake area without amplification; **b** curvature used to define topographic factors for seismic shaking, with factors of 0.8 in valleys and 1.5 on mountain tops; **c** Arias intensity map without and **d** with topographic amplification

1970). I_A was calculated using Eq. (1) proposed by Keefer et al. (1989), using the raster calculator in ArcGIS 10.5. I_A is expressed in meter per second^{-1}. This formula was also used by Havenith et al. (2006) in their analysis of seismotectonic and possible climatic influences of co-seismic landslides in the central Tien Shan.

$$logI_A = -4.1 + M - 2logR + 0.5P \qquad (1)$$

where M is the magnitude of the earthquake (6.8 for the 2022 Luding earthquake), and R is the mean distance from the epicenter and activated fault section. The amplified Arias intensity map of Luding (Fig. 5d) considers the topographic amplification which is the influence of the curvature computed before.

Methods: conception and computation process of scenarios

We compare the predictive power of M99 (Eq. 3) and J18 (Eq. 4) equations for SW China. We first determine whether the landslides' spatial distribution and sizes can be predicted more efficiently using either the simplified ND approach (M99 or Eq. 3) or a recent modified form (J18 or Eq. 4). Second, we evaluate the effect of site-specific conditions, such as slope orientation and topographic amplification, on these models. The predictive power of the computed ND scenarios was evaluated by determining the landslide proportion as the number of landslide pixels divided by the total pixels of the corresponding ND class. This evaluation method was also used by Jibson et al. (2000) and Ma and Xu (2019).

The general form of the traditional ND equation (Eq. 2) presents three terms or predictor variables: the first $X_1 logI_A$ represents the shaking intensity I_A, the second $X_2 A_c$ or $X_2*log(A_c)$ represents the critical acceleration (A_c), and the last term "X_3" represents the errors or uncertainties. The logarithmic critical acceleration ($logA_c$) was introduced into the modified ND equations (Eq. 4), which fits better than a linear term when performing regression with larger data set as highlighted by Jibson et al. (2000).

$$log(D) = X_1 \times logI_A - X_2 \times A_c + X_3 \qquad (2)$$

$$log(D) = 1.46 \times log(I_A) - 6.642 * A_c + 1.546 \qquad (3)$$

$$log(D) = 0.465 logI_A + 12.896 A_c logI_A - 22.201 A_c + 2.092 \pm 0.148 \qquad (4)$$

The two versions of the ND method proposed by M99 and J18, relate the displacement (D) to I_A and A_c. A_c is linked to the factor of safety (FS) and slope angle (α) by means of the acceleration due to gravity ($g = 9.81$ m/s²), as shown by Eq. 5 proposed by Keefer et al. (1989):

$$A_c = (FS - 1) \times g \times \sin \alpha \qquad (5)$$

FS is computed under the assumptions of the infinite slope model (Ward et al. 1982) using Eq. 6 proposed by Jibson et al. (2000):

$$FS = \frac{c}{\gamma \times t \times \sin\alpha} + \frac{\tan\varphi}{\tan\alpha} - \frac{m \times \gamma_w \times \tan\varphi}{\gamma \times \tan\varphi} \qquad (6)$$

In Eq. (6), c is the cohesion in kPa, φ the friction angle in degrees, γ the unit weight in kN/m³, and m the wetness or saturated part of the total potential sliding body.

A total of 46 scenarios were computed, 23 using M99 and 23 using J18, using the raster calculator of the ArcGIS 10.5 Spatial Analyst tools. The following variables are considered: sliding depth (5, 20, and 50 m), soil-rock geomechanical properties (total cohesion, angle of internal friction, unit weight, and wetness), site effects (slope orientation), and topographic amplifications (effect of curvature and mean distance to the epicenter and the seismogenic Moxi fault section). The ND models were computed for three co-seismic landslide types (shallow, deeper, and deep-seated), with thicknesses of the potential slip layer value "t" of 5, 20, and 50 m. These scenarios were calculated using the following geomechanical

property maps: cohesion (c in kPa), friction angle (φ in degrees), unit weight (γ in kN/m³), and wetness (m). We assigned the same geomechanical values to stable and unstable areas for all scenarios, because geomechanical properties values present in the literature on superficial geological formations (preferential place for triggering co-seismic landslides) do not vary significantly with lithology.

Kumar et al. (2021) highlighted that cohesion increases with depth. To simulate the triggering conditions for landslides in geological formations at greater depths (20 and 50 m), we assigned higher values to cohesion and friction angle. We considered three wetness or saturation states by assigning m values of 0, 0.5, and 1. The m values of 0 and 1 represent soil conditions in fully dry (no pore-water pressure) and fully saturated conditions, respectively. These wetness conditions simulate those observed during the completely dry and wet seasons, but also in between. The unit weight values considered are 18, 20, and 23 kN/m³. We therefore chose the following cohesion/friction angle pairs: 50 kPa/25°; 500 kPa/30°; 500 kPa/40°; 5000 kPa/30°; and 5000 kPa/40°.

We implemented 23 ND scenarios assuming shallow ($t = 5$ m), intermediate ($t = 20$ m), and deep landslides ($t = 50$ m), to account for the presence or absence of such landslides and predict their likely locations. The decision tree approach is used to partition the geomechanical parameters and slip depths (t, c, φ, γ, and m), as shown in Fig. 6. These 23 critical acceleration scenarios were then combined with each of the two ND equations, yielding a total of 46 predictions (online Appendix 2 of the supplementary material).

Results

Here, we present the spatial distribution of ND values and the assessment of the efficiency of scenarios with high variability of ND values.

Spatial distribution of Newmark displacement values

Appropriate thresholds for triggering the slope displacement vary between 5 and 10 cm as suggested by Jibson and Keefer (1993) and Cui et al. (2019). The ND maps were classified into six classes using the manual classification method. These classes are ND < 0.5, 0.5–2, 2–10, 10–25, 25–80, and ND ≥ 80 cm, where possible. These maps were classified into two groups: scenarios with high spatial variability (HSV) in ND values (Fig. 7a) and scenarios
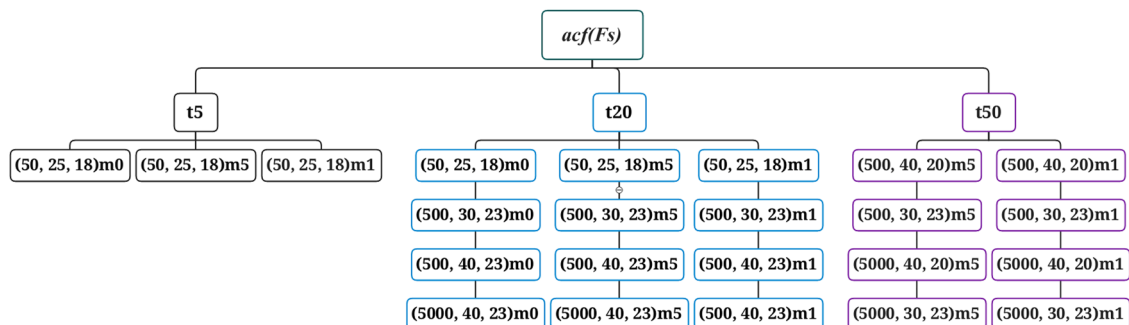
Fig. 6 Decision tree to compute the acceleration as a function of the factor of safety *acf(FS)*, where (50, 25, 18)*mX represents the combination of soil-rock geomechanical properties (*c*, φ, γ)mX used to define ND scenarios (*X* being 0, 0.5, or 1)

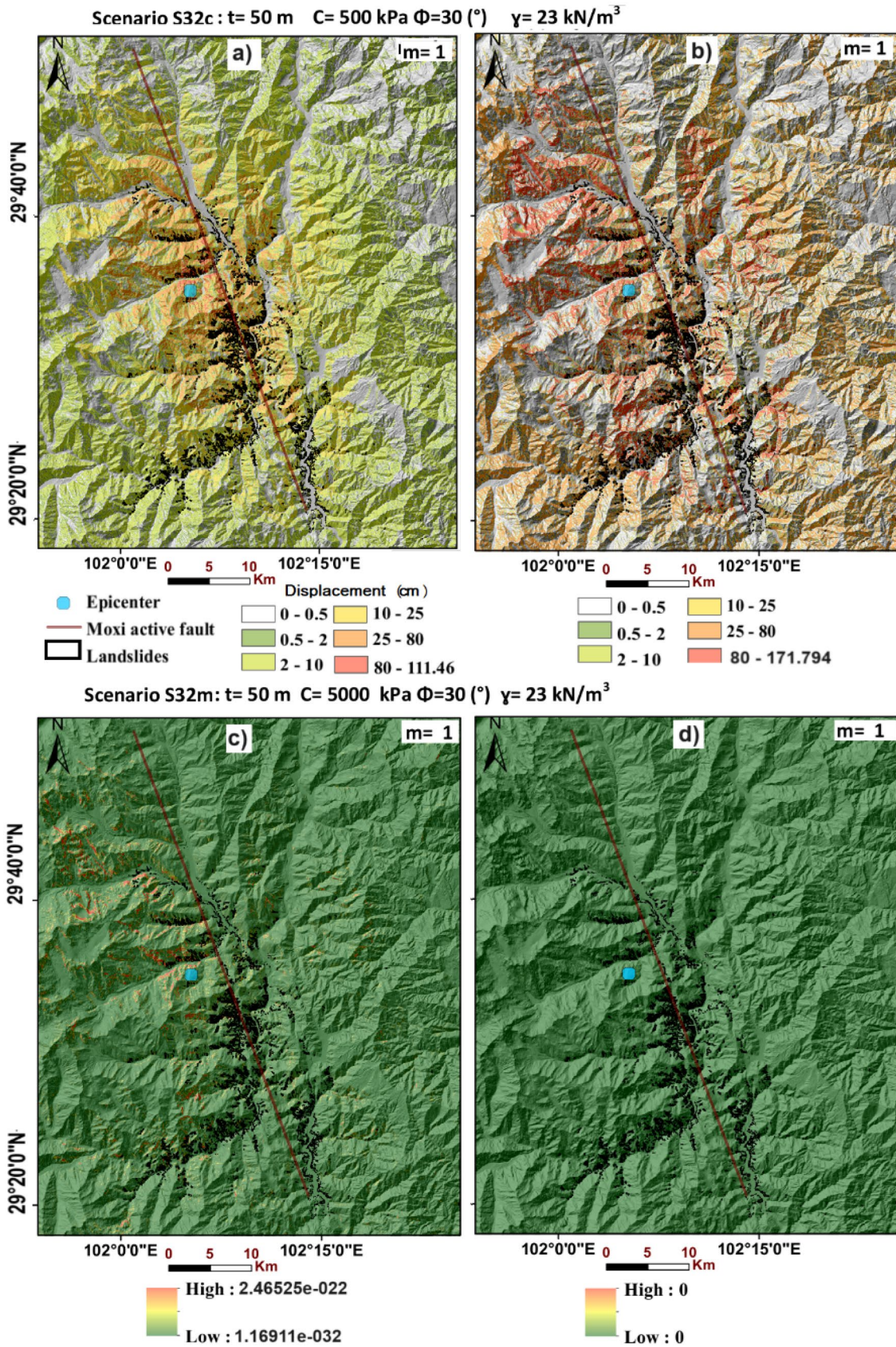Fig. 7 ND scenarios S32c and S32m with high spatial variability (HSV) from M99 (**a**) and J18 (**b**); low spatial variability (LSV) from M99 (**c**) and J18 (**d**)

with little or no variability (LSV) (Fig. 7b). Due to the small difference in the spatial distribution of ND values, only the maps of representative scenarios for each type of landslide are shown for each condition. Maps of the 46 scenarios without amplification and the 40 scenarios with topographic amplification and slope orientation calculated from the M99 and J18 equations are available in Portable Network Graphics (PNG) format in the supplementary material.

Ten scenarios out of the 23 computed (Table 1), displayed HSV of ND values (S1m, S2m, S31C, and S32C). These scenarios are consistent with the existence of landslides with the sliding depths used in the simulation, as shown below. This variability would also reflect the diversity existing between geomechanical and geoenvironmental (slopes, aspects, vegetation) conditions, the combination of which leads to the occurrence of landslides in a preferential zone.

These scenarios, which show LSV in ND (S22m, S22C, S23m, S31m, and S32m), reflect small displacements (~ 1 cm) throughout the map. This situation would reflect the absence of landslides with the sliding depths used in the simulation. The scenarios showing HSV of ND values include all scenarios simulating conditions suitable for triggering shallow landslides ($t = 5$ m). As well as 25% of scenarios assuming sliding depth ($t = 20$ m), and 50% of scenarios simulating favorable conditions for deep landslides ($t = 50$ m). This HSV was observed in identical scenarios using M99 and J18 Newmark equations.

Table 1 Newmark displacement scenarios with high and little/no spatial variability in values

Scenario		t (m)	c	φ (°)	γ (kN/m³)	m	Miles and Ho (1999)	Jin et al. (2018)
Scenarios with high-class variability								
S1m	S1m0	5	50	25	18	0	S1m_M99	S1m_J18
	S1m5	5		25	18	0.5		
	S1m1	5		25	18	1		
S2m	S21m0	20	50	25	18	0	S21m_M99	S21m_J18
	S21m5	20		25	18	0.5		
	S21m1	20		25	18	1		
S31C	S31c5	50	500	40	20	0.5	S31c_M99	S31c_J18
	S31c1	50		40	20	1		
S32C	S32c5	50	500	30	23	0.5	S32c_M99	S32c_J18
	S32c1	50		30	23	1		
Scenarios with less or no class variability								
S22m	S22m0	20	500	30	23	0	S22m_M99	S22m_J18
	S22m5	20		30	23	0.5		
	S22m1	20		30	23	1		
S22C	S22c0	20	500	40	23	0	S22c_M99	S22c_J18
	S22c5	20		40	23	0.5		
	S22c1	20		40	23	1		
S23m	S23m0	20	5000	40	23	0	S23m_M99	S23m_J18
	S23m5	20		40	23	0.5		
	S23m1	20	5000	40	23	1		
S32m	S32m5	50	5000	30	23	0.5	S32m_M99	S32m_J18
	S32m1	50		30	23	1		
S31m	S31m5	50	5000	40	20	0.5	S31m_M99	S31m_J18
	S31m1	50		40	20	1		

Comparison between Newmark displacement values for scenarios without amplification and those under topographic amplification

The results of scenarios without amplification are presented together with those that consider the influence of the topographic amplification to highlight the effect of the latter. S1mX, S21mX, and S32cX refer to scenarios without amplification, while S1mXa, S21mXa, and S32cXa denote those with topographic amplification.

Scenarios simulating suitable conditions for shallow landslides with t = 5 m, c = 50 kPa, Φ = 25°, and γ = 18 kN/m^3
Scenarios S1mX (Fig. 8a–d) and S1mXa (Fig. 8e–h) predict high ND values only for near-fault sites when the M99 equation (Fig. 8a, b, e, and f) is used. These values decrease with distance from the epicenter. However, high ND values are dominant over the Luding area, also for sites far away from the activated fault segment when using the J18 equation (Fig. 8c, d, g, and h). These high values are observed in both the unamplified and amplified scenarios. ND values close to zero under normal conditions become very high (between 25 and ~200 cm) under amplification.

Scenarios simulating suitable conditions for medium-depth landslides with t = 20 m, c = 50 kPa, Φ = 25°, and γ = 18 kN/m^3
These correspond to scenarios S21mX (Fig. 8a–d) and S1mXa (Fig. 9e–h). High ND values are more abundant around the fault and epicenter (red). Low displacements (green and yellow) gradually increase with distance for M99 (Fig. 9a, b, e, and f). Similar to scenarios simulating suitable conditions for shallow landslides, larger ND values are distributed over the whole area even far away from the fault and epicenter when using the J18 equation (Fig. 9c, d, g, and h). However, under amplification, slight differences are observed at the level of the spatial distribution of ND classes symbolized by minor changes in color.

Scenarios simulating suitable conditions for deep landslides computed with t = 50 m, c = 500 kPa, Φ = 30°, γ = 23 kN/m^3
These correspond to scenarios S32c (Fig. 10a–d) and S1mXa (Fig. 10e–h) considered as representative. Similar to shallow and medium-depth landslide scenarios, higher ND values also concentrate near the fault for M99 (Fig. 10a, b, e, and f). For J18, higher ND values are again distributed over the entire zone, even far away from the fault and the epicenter (Fig. 10c, d, g, and h).
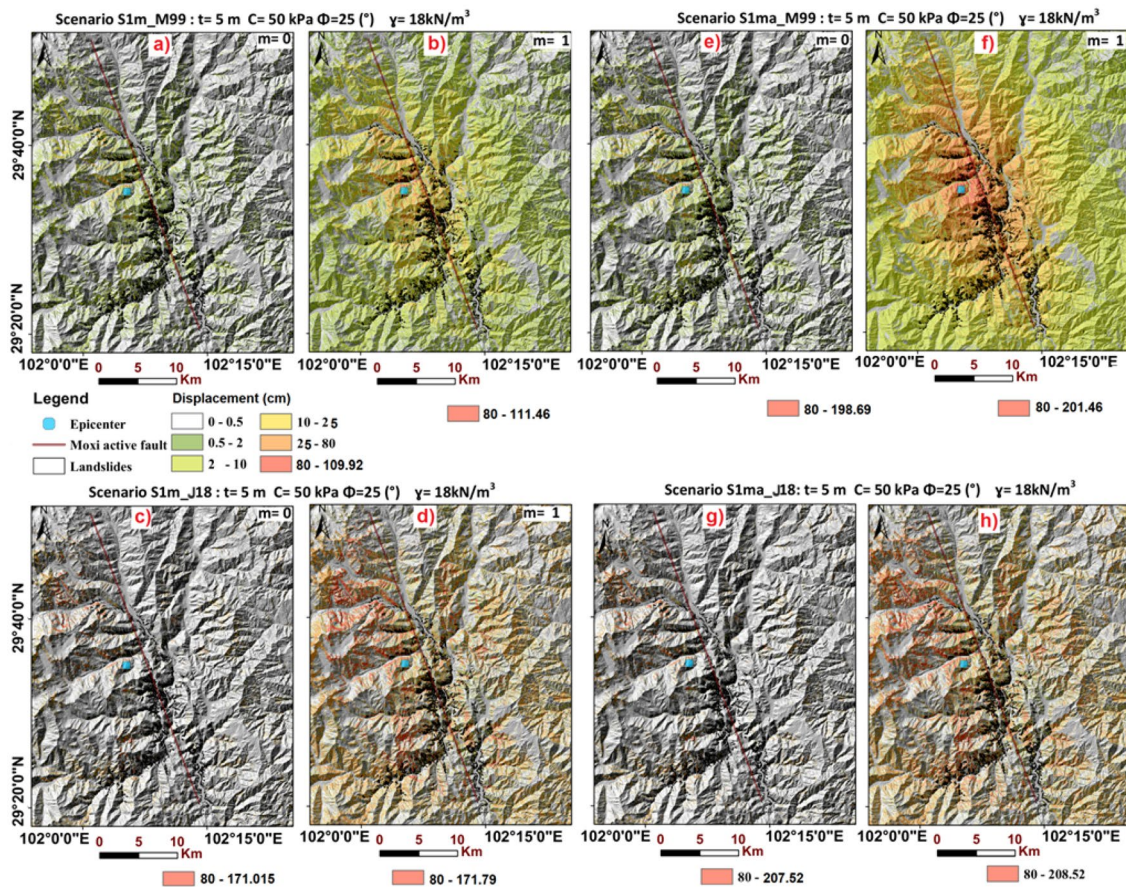
Fig. 8 ND scenarios S1mX (**a** to **d**) and S1mXa (**e** to **h**). Scenarios S1mX_M99 and S1mXa_M99 (**a**, **b**, **e**, and **f**) result from the M99 equation, and scenarios S1mX_J18 and S1mXa_J18 from the J18 equation (**c**, **d**, **g**, and **h**), with factor *m* (saturation) increasing from left (*m* = 0) to right (*m* = 1)
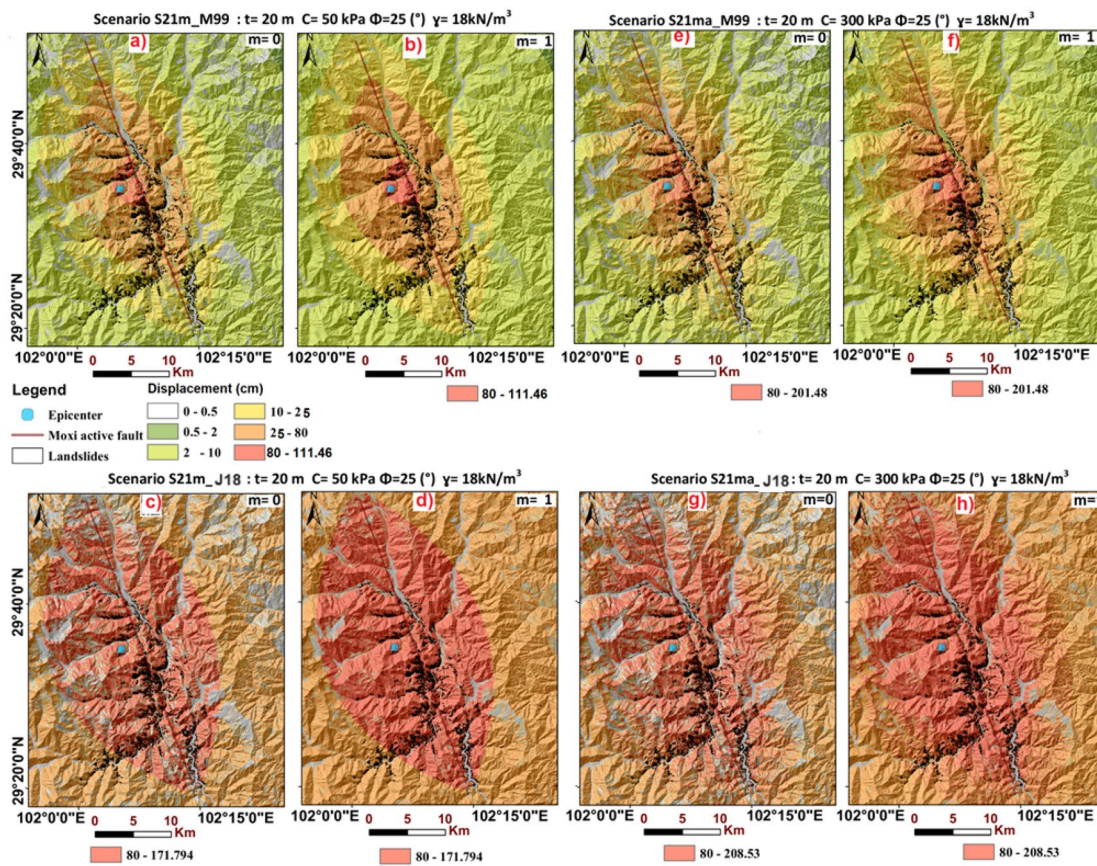
Fig. 9 ND scenarios S21mX (**a** to **d**) and S21mXa (**e**, **f**). Scenarios S21mX_M99 and S21mXa_M99 (**a**, **b**, **e**, and **f**) result from the M99 equation, and scenarios S21mX_J18 and S21mXa_J18 from the J18 equation (**c**, **d**, **g**, and **h**)

This distribution does not depend on the degree of saturation or the change in soil-rock geomechanical properties so that the topographic amplification does not significantly affect the ND spatial distribution.

The highest ND values increase from left to right with increasing m values (Figs. 8, 9, and 10). The scenario on the left in these Figs. 8, 9, and 10 represent dry ($m = 0$), and that on the right represents fully saturated ($m = 1$) wet conditions. Predicted displacements from M99 range from 0 to ~110 cm for all saturated scenarios without amplification. Considering topographic amplification, we obtain ~200 cm. These displacement values vary between 0 and 172 cm for all wetness or saturation conditions when using the J18 equation without amplification (Figs. 8, 9, and 10). The highest ND value of 209 cm is obtained under the topographic amplification. The low ND values (green and yellow colors in Figs. 8, 9, and 10) are gradually and more widely distributed with increasing m. Whereas for J18, larger ND values appear immediately far from the fault in full saturation ($m = 1$). Moreover, ND values predicted by using the J18 equation are marked by very high values, from 25 to ~200 cm. These values might reflect the high sensitivity of J18 to any change in A_c. J18 seems to stress more the importance of slope stability factors (FS and A_c) than the ground shaking intensity (I_A), which is more uniformly distributed.

Scenarios showing little or no variability of ND values

Scenarios with larger potential slip layer value t (20 m, and mostly 50 m), c (500 and generally 5000), Φ (30°, and mostly 40°) values, display very low ND values (~1 cm) or zero (supplementary material). These low ND values are observed when using both M99 and J18. These low displacements would reflect the absence of larger landslides with a deeper sliding surface ($t \geq 20$) that would cross harder rocks. Those simulations thus confirm that this M_s 6.8 earthquake was not strong enough to cause such deep landslides in harder rocks, as observed in the field.

Efficiency assessment of scenarios showing high variability of ND values

The predictive power of all ND scenarios showing high spatial variability was evaluated by determining the proportion of landslide pixels within each ND class (Fig. 11a–h). Landslide proportion is the number of landslide pixels divided by the total pixels of the corresponding ND class (Jibson et al. 2000; Ma and Xu 2019). We only present one representative scenario for shallow and moderate and two for deep-seated landslides. These curve shapes are identical
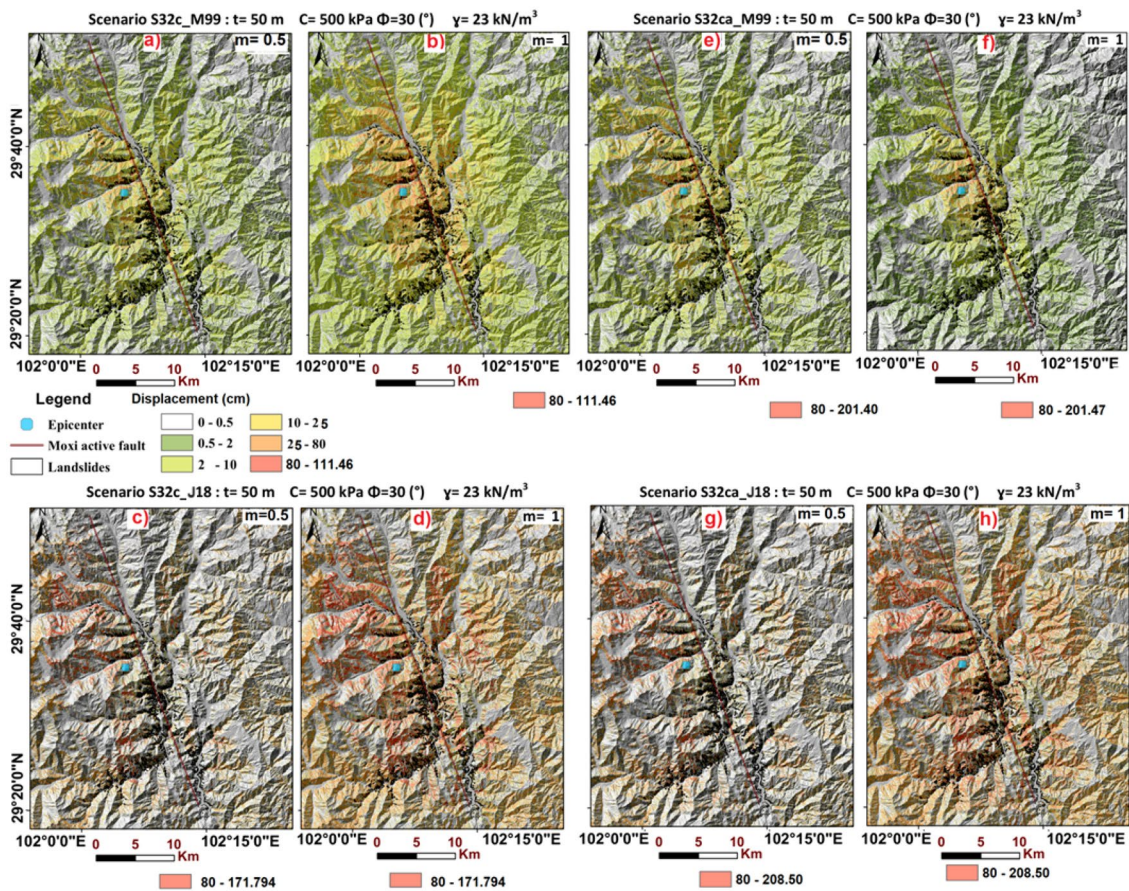
Fig. 10 ND scenarios S32cX (**a–d**) and S32cXa (**e**, **f**). Scenarios 32cX_M99 and 32cXa_M99 (**a**, **b**, **e**, and **f**) result from the M99 equation, and scenarios 32c_J18 and 32cXa_J18 from the J18 equation (**c**, **d**, **g**, and **h**)

in other scenarios with HSV with or without amplification. The validation curves of scenarios showing low or no spatial variability of ND values were not computed. To highlight the topographic amplification effect, the predictive capacities of scenarios without amplification are presented together with those considering the topographic amplification influence.

Scenarios computed with the Miles and Ho's (1999) equation
The proportion of landslide pixels increases continuously with ND values for all scenarios computed with the M99 equation (Fig. 11a–h). This proportion increases slowly between 0.5 and 25 cm. A jump is observed from 25 cm to ND ≥ 80 cm. However, several peculiarities are observed in this relationship as presented below.

(a) Scenarios simulating suitable conditions for shallow landslides
These scenarios include S1m_M99 and S1ma_M99 computed with $t = 5$ m, $c = 50$ kPa, $\Phi = 25°$, and $\gamma = 18$ kN/m³. The highest landslide proportion of 14% is observed for ND ≥ 80 cm in the S1m5_M99 assuming moderate wetness ($m = 0.5$) without amplification. Considering the topographic amplification, this highest proportion decreases to 9%. This proportion is observed for ND ≥ 80 cm in S1ma0_M99 and S1ma5_M99, assuming medium and dry wetness conditions (Fig. 11a, e).

(b) Scenarios simulating suitable conditions for medium-depth landslides
These scenarios include S21m_M99 and S21ma_M99 calculated with $t = 20$ m, $c = 50$ kPa, $\Phi = 25°$, and $\gamma = 18$ kN/m³. The highest landslide proportion of 6% is observed for ND ≥ 80 cm in S21m0_M99 assuming dry conditions without amplification. Under topographic amplification, the highest proportion decreases to 5% in S21ma_M99 (Fig. 11b, f).

(c) Scenarios simulating suitable conditions for deep landslides
These include two scenarios: S31c_M99 and S31ca_M99 (with $t = 50$ m, $c = 500$ kPa, $\Phi = 40$ (°), $\gamma = 20$ kN/m³), and S32c_M99 and S32ca_M99 (with $t = 50$ m, $c = 500$ kPa, $\Phi = 30°$, $\gamma = 23$ kN/m³). For the first, the highest landslide proportions of 14% for ND ≥ 80 cm are obtained without amplification (S31c5_M99) and 8% under topographic amplification (S31c5a_M99) (Fig. 11c, g). Regarding the second deep landslide scenario (Fig. 11d, h), the highest landslide proportion of 13% is observed in S32c5_M99 and 8% under topographic amplification (S32c5a_M99), assuming moderate wetness ($m = 0.5$).

Scenarios calculated using the equation of Jin et al. (2018)
There is a discontinuous evolution between the ND values and the proportion of landslides for all the scenarios (Fig. 11a–h), regardless of having topographic amplification or not. This landslide
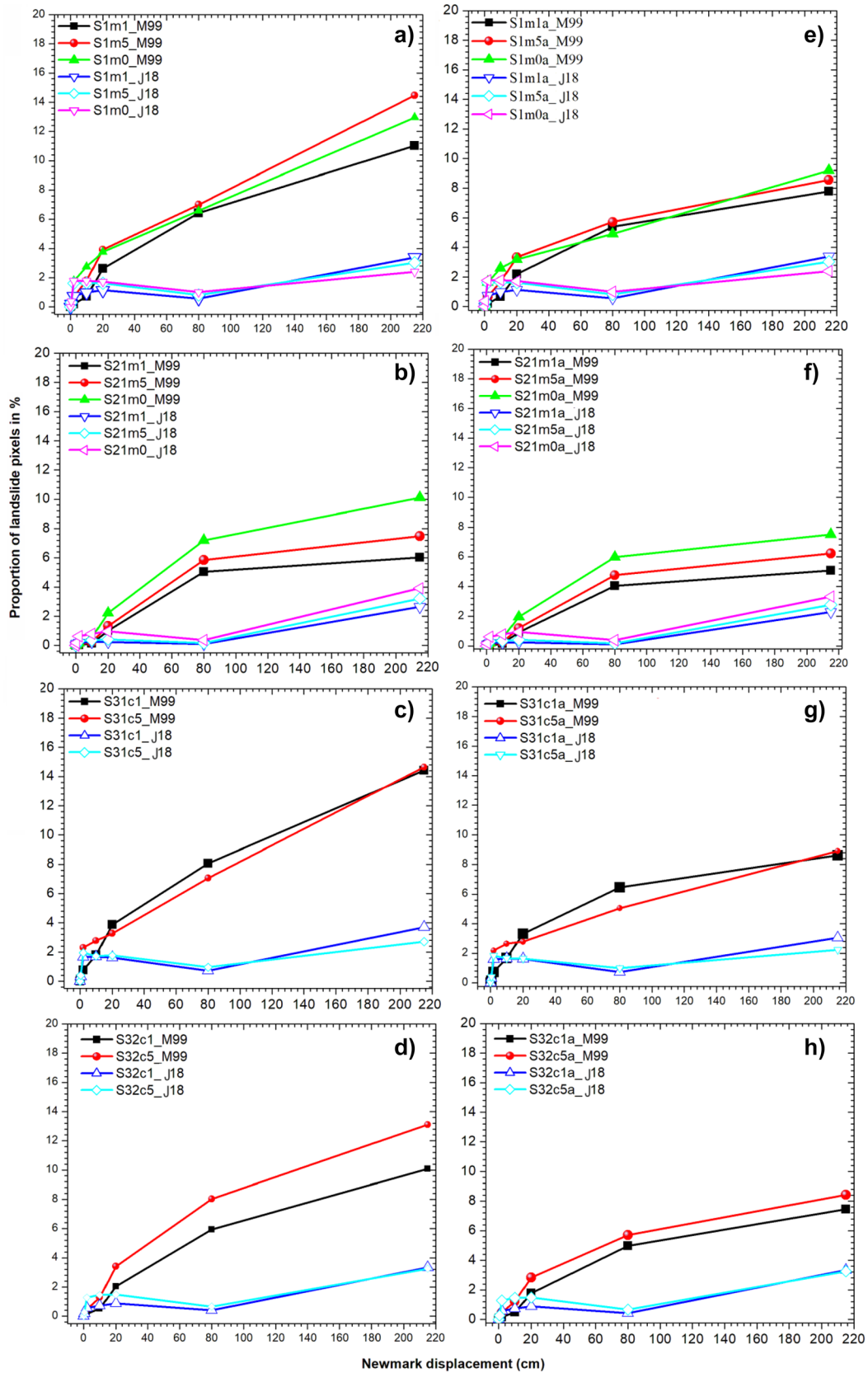
Fig. 11 Landslide proportion as a function of the ND for scenarios without amplification (**a**–**d**) and those with topographic amplification (**e**–**h**)

proportion first increases slowly between 0.5 and 2 cm before remaining constant up to 25 cm. It decreases between 25 and 80 cm and increases again from ND ≥ 80 cm. Peculiarities observed in this relationship are presented below.

(a) Scenarios simulating suitable conditions for shallow landslides

The highest landslide proportion captured is 4% in S1m1_J18 and S1m5_J18 assuming fully saturated and medium wetness conditions, with and without amplification (Fig. 11a, e).

(b) Scenarios simulating suitable conditions for medium-depth landslides

These include S21m_J18 and S21ma_J18. The highest landslide proportion of 4% is also observed assuming fully saturated and medium wetness conditions without amplification. Under topographic amplification, this ratio drops to 2% (Fig. 11b, f).

(c) Scenarios simulating suitable conditions for deep landslides

These include S31c_J18 and S31ca_J18 followed by S32c_J18 and S32ca_J18. For the first, the highest landslide proportions of 3% are obtained without amplification (S31c_J18). Under topographic amplification, this ratio drops to 2% in S31ca_J18 (Fig. 11c, g). For the second, the highest landslide

proportions of 3% are obtained in all wetness conditions with and without amplification in S32c_J18 and S32ca_J18 (Fig. 11d, h).

Discussion

This section focuses first on the comparison of the predictive power of the Miles and Ho (1999) and the Jin et al. (2018) equations and the influence of topographic amplification. A second section comments on the preferential spatial distribution of landslides, which was found during the analysis of all scenarios.

Comparison of the predictive power of Miles and Ho (1999) and Jin et al. (2018) equations

The predictive power of all ND scenarios showing high spatial variability, as evaluated previously in the "Efficiency assessment of scenarios showing high variability of ND values" section, allowed determining the proportion of landslide pixels within each ND class. Figure 12a and b shows this proportion as a function of ND for shallow landslides, whose curve shape is identical in other scenarios, with or without amplification.
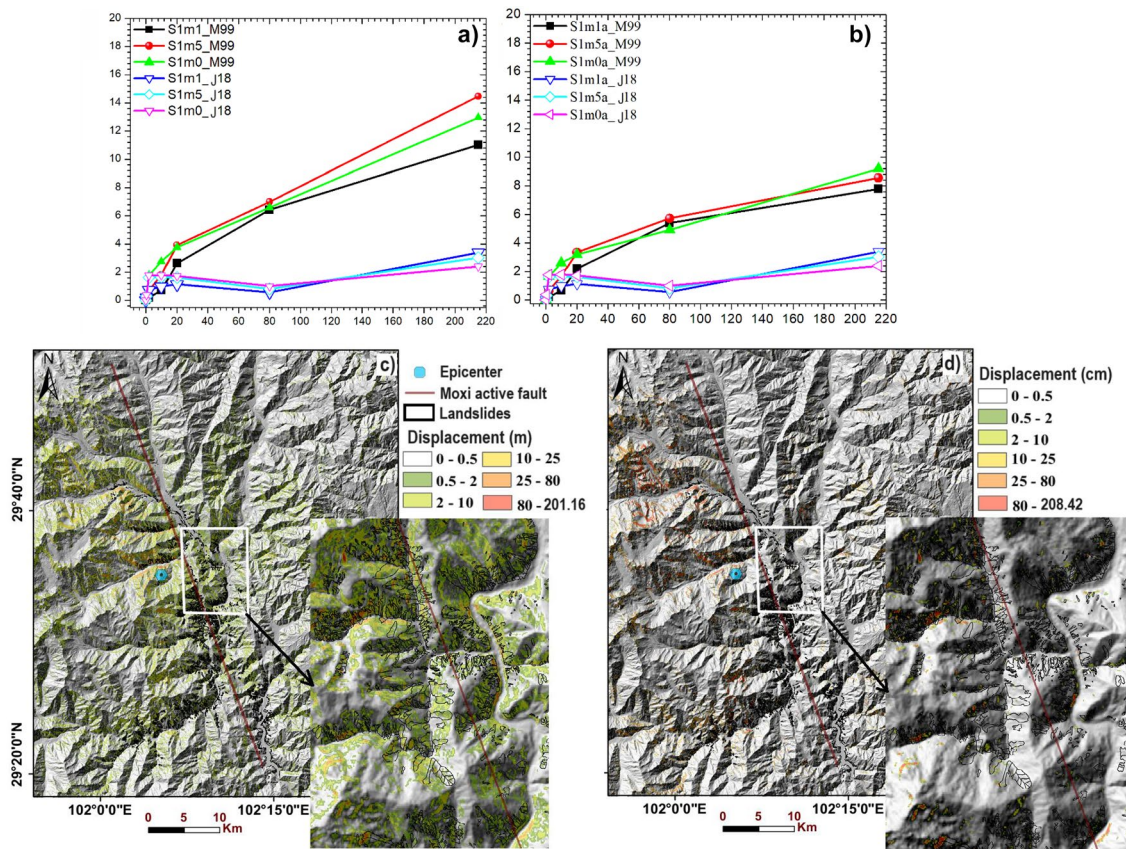

Fig. 12 Scenarios S1mX and S1mXa showing landslide proportion as a function of the ND **a** without amplification and **b** under topographic amplification; **c** calculated with M99 equation; and **d** computed with J18 with $t = 5$ m, $c = 50$ kPa, $\Phi = 25°$, and $\gamma = 18$ kN/m³. Higher ND values can be observed on slopes with few landslides on the enlarged parts of the image

The validation curves of the scenarios resulting from these two equations define two different sets, with the curves resulting from M99 at the top, and those resulting from J18 at the bottom. The scenarios calculated with J18 tend to capture fewer landslides than M99, considering the same ND classes without amplification (Fig. 12a). Scenarios computed with J18 considering topographic amplification also capture less landslides than when using M99 (Fig. 12b). The J18 equation stresses more the importance of local slope stability with a high A_c coefficient of 22.201 and the product $(A_c * \log I_A)$. The seismic effects are therefore reduced, leading to poor modeling of the spatial distribution of landslides. Consequently, very high ND values are observed far from the seismogenic fault and epicenter, where there are no more landslides (Fig. 12c, d). J18 seems less suitable for earthquakes with high landslide concentration in the epicentral region, as observed in the Luding case.

The highest landslide proportion of 14% is observed for ND ≥ 80 cm in the scenario without amplification (curve s1m5_M99). However, the highest proportion of landslides, 9%, is observed for ND ≥ 80 cm, considering the topographic amplification (curve s1m0_M99). Therefore, it can be followed that the topographic effect does not improve prediction. Likely because few or no massive landslides were triggered from mountain peaks. The scenario S1mX, simulating shallow landslides, is considered a representative for M99 and J18 equations (Fig. 12). However, the predictive ability of these models remains limited by the high ND values obtained on north and west-facing slopes (Fig. 12c, d). This leads to an underestimation of these values on east and south-facing slopes.

Influence of the preferred spatial distribution of landslides

The spatial distribution of landslides induced by the Luding earthquake presents a preferential location in the E-, SE-, and S-facing slopes as pointed out by Dai et al. (2023), Liu et al. (2023), and Xiao et al. (2023). However, the ND models without amplification present high ND values instead on N- and W-facing slopes. An underestimate of these displacement values is therefore observed on E- and S-facing slopes. This leads to the presence of landslides in areas where the predicted permanent displacement values are very low, as noticed before in Fig. 12. This effect has therefore been corrected by applying the amplification factor for slopes with aspects > 90° and < 220° in ArcGIS 10.1. This was similarly done for curvature, by amplifying the I_A map by 1.5 for E- and S-facing slopes (between 80° and 220°), 1 for intermediate slopes (40–80°; 220–260°), and attenuating by 0.7 for W- and N-facing slopes (260–40°). The resulting I_A map considering slope orientation amplification influence factors for seismic shaking is shown in Fig. 13. This amplified I_A was therefore used to compute new ND scenarios under the slope aspect influence.

Effect of slope orientation on ND scenarios

The predicted displacements with slope orientation amplification for all scenarios calculated using the M99 equation range from 0 to ~ 200 cm (Fig. 14C, D), which is twice the value obtained without amplification (110 cm). The same values were obtained under
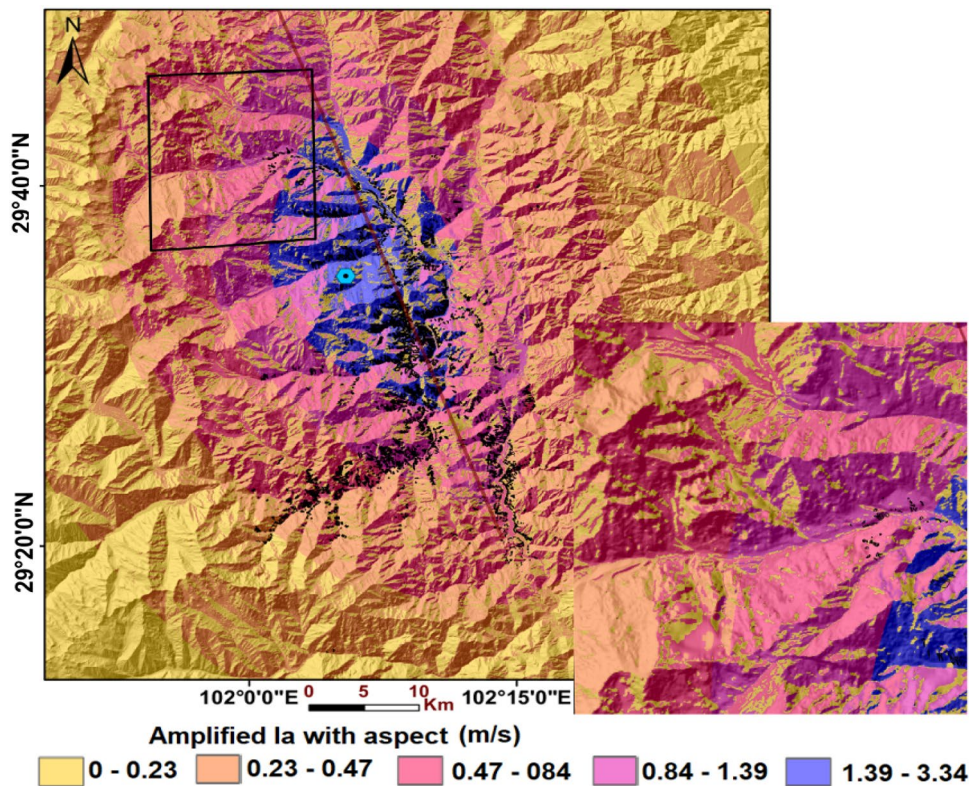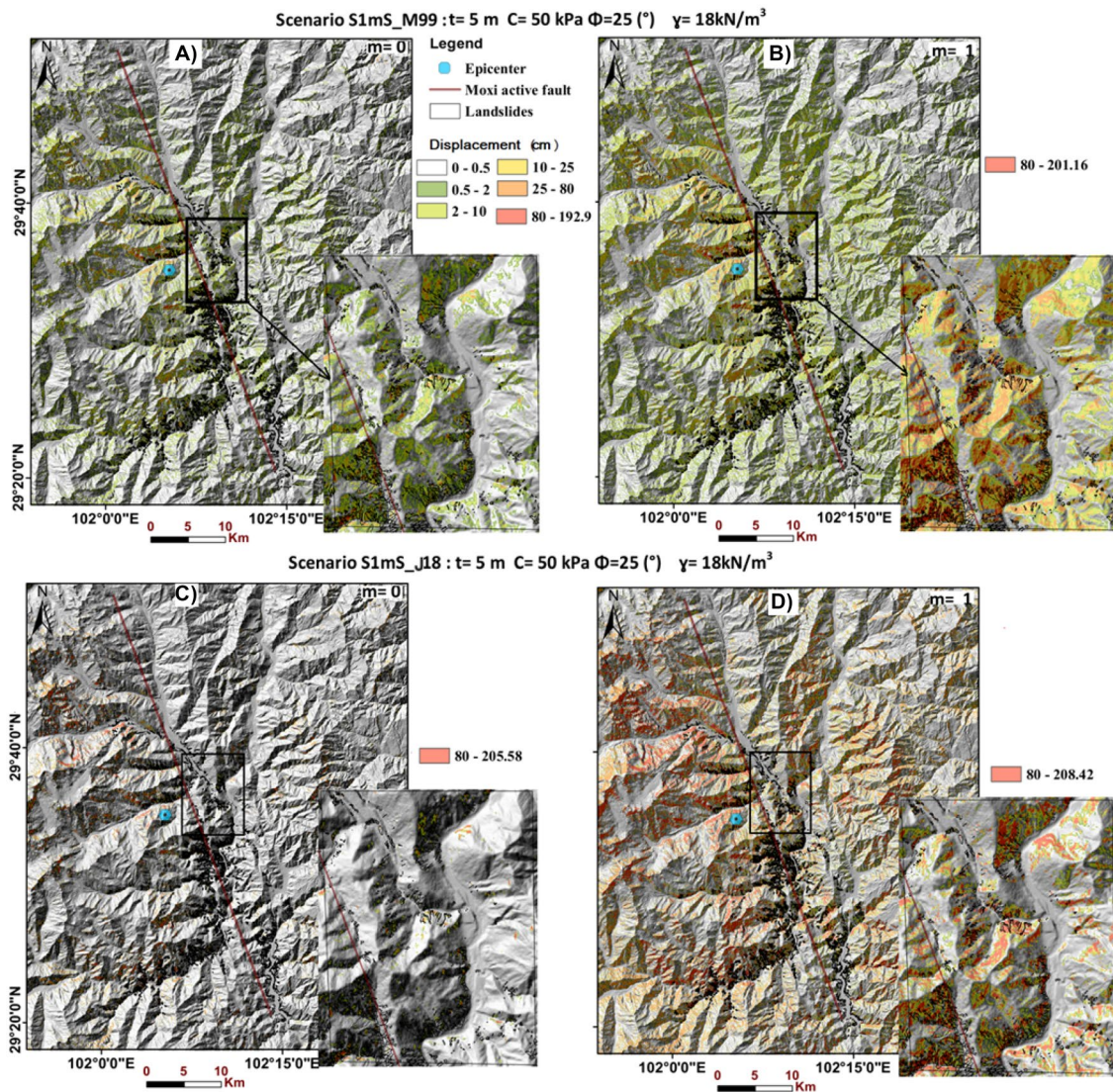

Fig. 13 Arias intensity (I_A) map of Luding earthquake area considering the slope orientation influence

Fig. 14 Slope amplification effects on ND scenarios: case of S1mXS calculated with $t=5$ m, $c=50$ kPa, $\Phi=25°$, and $\gamma=18$kN/m^3; where **A** and **B** are calculated using the M99 equation; **C** and **D** are calculated using the J18 equations

topographic amplification, although the resulting ND values are distributed differently. The ND values increase with saturated conditions: from 0 to ~193 cm in dry, 0 to 199 cm for moderate wetness, and 0 to 201 cm in fully saturated conditions (Fig. 14).

Scenarios calculated with J18 show ND values varying between 0 and ~209 cm, i.e., very similar to those obtained with topographic amplification, and slightly greater than the 172 cm obtained without amplification (Fig. 14A, B). Thus, slope orientation and topographic amplifications increase the ND values calculated without amplification using M99 and J18 equations. The spatial distribution of ND values observed in scenarios S1mS_M99 and S1mS_J18 (Fig. 14) is similar to that observed in all other scenarios (supplementary material). All other scenarios with high spatial variability present similar discrepancy between ND values, regardless of variations in geotechnical properties and moisture conditions.

**Performance of ND scenarios with slope orientation amplification**

The validation curves of ND scenarios with slope orientation amplification show that J18 still captures fewer landslides than M99 (Fig. 15).

**Scenarios computed with Miles and Ho's (1999) equation**
The validation curves of scenarios computed with M99 have the same monotonous behavior as those obtained without amplification and under the topographic amplification (Fig. 15).

The scenarios simulating suitable conditions for shallow-depth landslides display the highest landslide proportion of 19% for ND ≥ 80 cm in S1ms0_M99 and S1ms5_M99 assuming medium and dry conditions (Fig. 15a, e). These values are slightly higher
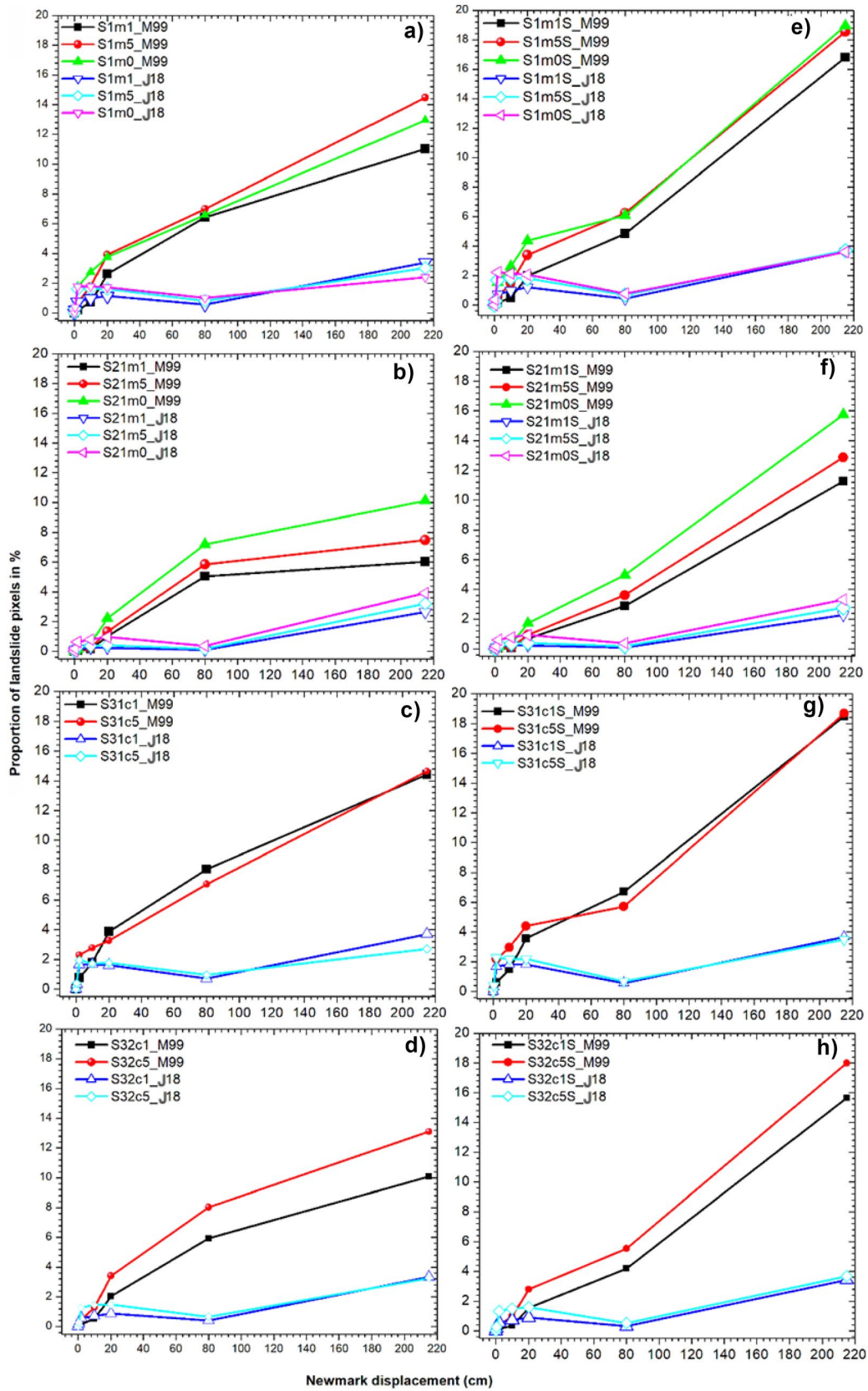
Fig. 15 Landslide proportion as a function of the ND for scenarios without amplification (**a–d**) and those with slope orientation amplification (**e–h**)
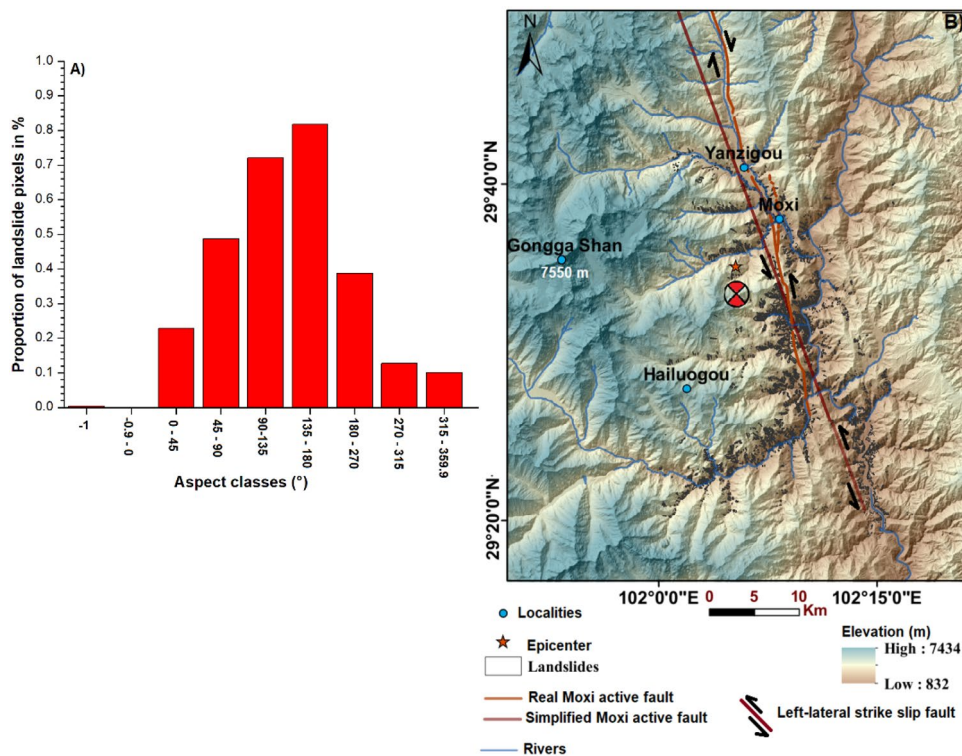
Fig. 16 Landslide preferential distribution: **A** Variation of landslide proportions as a function of slope orientation (landslides dominate between 45–90°, 90–135°, 135–180°, and 180–270° corresponding to NE, E, SE, S, and SW directions); in scenarios without amplification (red bars), scenarios under topographic amplification; **B** Extension of the Luding landslides in an NW–SE direction following the left-lateral strike-slip Moxi fault

than the highest landslide proportions of 13 and 14% obtained under medium and dry wet conditions in scenarios without amplification. Moreover, these values are also higher than the highest proportion of 9% obtained in the same wetness conditions under topographic amplification.

The scenarios simulating suitable conditions for medium depth landslides, show the highest landslide proportions of 11 and 12%. These values are observed in S21ms0_M99 and S21ms5_M99 assuming medium and dry wet conditions (Fig. 15b, f). These proportions are higher than the highest landslide proportions of 6 and 5% observed without amplification and under topographic amplification, respectively.

The scenarios simulating suitable conditions for deep landslides include S31cs_M99 and S32cs_M99. The highest landslide proportions of 19% are obtained in the first deep landslide scenario S31c5s_M99 for ND ≥ 80 cm, assuming dry conditions (Fig. 15c, g). The highest landslide proportions for the second deep landslide scenario S32c5s_M99 is 18, assuming dry conditions (Fig. 15c, g). These proportions are still higher than the 15 and 10% obtained in the same scenarios without amplification and with topographic amplification, respectively.

Scenarios calculated using the equation of Jin et al. (2018)   The validation curves from J18 under slope orientation amplification have the same discontinuous evolution as those obtained without amplification and under the topographic amplification (Fig. 15). Under

slope orientation amplification, the highest landslide proportion of 4% is observed for ND ≥ 80 cm for all scenarios, assuming shallow, medium, and deep landslides, regardless of saturation conditions. The curves from J18 correspond to the set curves in the lower part of the graph (Fig. 15e–h). This proportion is similar to the 4 and 3% obtained in scenarios without amplification and considering the topographic amplification, respectively. Therefore, the topographic and slope orientation amplifications improve the prediction capacity of scenarios calculated with M99. These amplifications do not have any effect when using J18. In general, the model with slope orientation amplification works better (Fig. 15), probably due to the preferential distribution of landslides on E-, SE-, NE-, S-, and SW-facing slopes, as also highlighted by Dai et al. (2023). This preferential location might be either explained by the existence of an unequal distribution of vegetation related to aspect, or by the fault's focal mechanism, as also suggested by Chen et al. (2023) and Yang et al. (2023).

Uneven distribution of vegetation or focal effect mechanism of the fault to explain the preferential location of landslides on the SE-facing slopes?

The possible causes of the preferential landslide location are discussed with respect to the possible uneven distribution of the vegetation, structural, and seismotectonic influences. The assumption of an unequal distribution of vegetation by aspect was first formulated to adjust the ND scenarios to the preferential distribution of landslides

on the E-, SE-, and S-facing slopes. The slope orientation and the normalized difference vegetation index (NDVI) are geoenvironmental factors or specific site conditions used to explain this landslide pattern. The proportion of landslides as a function of aspect revealed a preferred spatial distribution of the latter on NE (0–45°), E (45–90°), SE (90–135°), S (135–180°), and SW (180–270°) facing slopes (Fig. 15a). These landslide percentages are 23% for NE, 49% for E, 72% for SE, 82% for S, and 39% for SW slope aspects. The NDVI is an index used to quantify the vegetation density (Appendix 3). The NDVI was derived from high-resolution Planet images of 3 m resolution acquired on July 5 and 6, 2022, following Eq. (7), as also used by Nsengiyumva et al. (2019), Khaple et al. (2021), and Prajisha et al. (2023). The first study assessed vegetation biomass and carbon stocks using a geospatial approach, while the second modeled landslide susceptibility using a generalized linear model in India. This index was also used by Huang et al. (2021) in the era of popular remote sensing.

$$NDVI = \frac{NIR - RED}{NIR + RED} \tag{7}$$

where NIR is the near-infrared band and RED is the red band.

A histogram showing the distribution of the proportion of pixels with higher NDVI classes as a function of the aspect classes is shown in Appendix 4. The distribution of vegetation on these slopes is somewhat uneven: flat (3%), northwest (85%), north (85%), east (84%), and south (86%). The preferential distribution of landslides on NE-, E-, SE-, S-, and SW-oriented slopes seems unrelated to an uneven spatial distribution of the vegetation. The Moxi fault focal mechanism might justify this landslide distribution as seen in Fig. 16B. The left-lateral strike-slip nature of the seismogenic Moxi fault resulted in maximum ground motion displacements in the NW–SE direction, as pointed out by Dai et al. (2023), Yang et al. (2023), Chen et al. (2023), and Li et al. (2022).

However, the following limitations of this study should be highlighted: soil-rock geomechanical properties, geoenvironmental, and seismic data used to compute ND equations were derived from previous studies. The infinite slope model has not yet been applied to large landslides at depths greater than 20 m. The failure surface and the ground water table of the Luding area were assumed to be parallel to the surface. The slopes were assumed to be homogeneous.

Conclusion

We compared the predictive performance of a traditional and an improved version of the Newmark displacement (ND) method. We have integrated the topographic and slope orientation amplifications to analyze the co-seismic landslides induced by the 2022 Ms 6.8 Luding earthquake in western Sichuan and eastern Tibetan Plateau. These landslides offer a good opportunity to check whether modifications made over decades really allowed obtaining ND equations applicable in regions other than those from which they originated.

The Miles and Ho (1999) or M99 equation was found to have a good ability to capture observed landslides, suggesting that it can consider both slope stability and seismic intensity. Contrarily, the equation from Jin et al. (2018) or J18 does not sufficiently consider the I_A attenuation effect, but rather, has a greater emphasis on slope stability inherent factors. Therefore, we suggest that the M99 equation is more suitable for earthquakes like that of Luding, with high landslide concentration in the epicentral region.

The Luding co-seismic landslides are best captured by scenario S1mX which simulates suitable conditions for shallow landslides, together with scenarios S31cX and S32cX for deep landslides. The topographic amplification does not improve the predictive capacity for both equations, possibly because no massive landslides were triggered from mountaintops. However, the inclusion of slope orientation increases the predictive power of both equations, consistent with the preferential distribution of landslides on E-, SE-, and S-facing slopes. It is also consistent with the NW-striking left-lateral Moxi seismogenic fault.

In the case of earthquakes, co-seismic landslide-prone areas, along with the likely size of landslides, can more efficiently be predicted using the ND method. Such method is also quicker to implement compared to statistical methods, as their execution depends on obtaining the landslide inventory. By contrast, the ND method can be implemented immediately when information on the epicenter, hypocenter, and seismogenic fault is available. They do not require to first conduct a landslide inventory, which generally depends on the time to obtain high-resolution satellite images of the pre- and post-seismic periods, as well as on the presence or absence of clouds such as in statistical methods.

Data availability

The data that support the findings of this investigation are available on request from the corresponding authors.

Declarations

Competing interests The authors declare no competing interests.

References

Allen CR, Luo Z, Qian H, Wen X, Zhou H, Huang W (1991) Field study of a highly active fault zone: the XSF of southwestern China. Geol Soc Am Bull 103:1178–1199. https://doi.org/10.1130/0016-7606(1991)103%3c1178:FSOAHA%3e2.3.CO;2

Akkar S, Sandıkkaya MA, Bommer JJ (2014) Empirical ground-motion models for point- and extended-source crustal earthquake scenarios in Europe and the Middle East. Bull Earthq Eng 12(1):359–387. https://doi.org/10.1007/s10518-013-9461-4

Anderson JG (2003) Earthquakes and engineering seismology., Academic Press, Volume 81, Part B, Editor(s): William H.K. Lee, Hiroo Kanamori, Paul C. Jennings, Carl Kisslinger, International Geophysics, Pages 937-p8, ISSN 0074-6142, ISBN 9780124406582. https://doi.org/10.1016/S0074-6142(03)80171-7

Arias A (1970) A measure of earthquake intensity. In: Hansen RJ (ed) Seismic design for nuclear power plants. Massachusetts Institute of Technology Press, Cambridge, MA, pp 438–483

Assimaki D, Gazetas G, Kausel E (2005) Effects of local soil conditions on the topographic aggravation of seismic motion: parametric investigation and recorded field evidence from the 1999 Athens earthquake. Bull Seismol Soc Am 95(3):1059–1089. https://doi.org/10.1785/0120040055

Athanasopoulos GA, Pelekis PC, Leonidou EA (1999) Effects of surface topography on seismic ground response in the Egion (Greece) 15 June 1995 earthquake. Soil Dyn Earthq Eng 18(2):135–149

Bai M, Chevalier M-L, Leloup PH, Li H, Pan J, Replumaz A et al (2021) Spatial slip rate distribution along the SE Xianshuihe fault, eastern Tibet, and earthquake hazard assessment. Tectonics 40:e2021TC006985. https://doi.org/10.1029/2021TC006985

Bai M, Chevalier ML, Pan J, Replumaz A, Leloup PH, Métois M, Li H (2018) Southeastward increase of the late Quaternary slip-rate of the Xianshuihe fault, eastern Tibet. Geodynamic and seismic hazard implications. Earth Planet Sci Lett 485:19–31. https://doi.org/10.1016/j.epsl.2017.12.045

Bertrand E, Duval AM, Régnier J, Azzara RM, Bergamaschi F, Bordoni P, Cara F, Cultrera G, Di Giulio G, Milana G, Salichon J (2011) Site effects of the Roio basin, L'Aquila. Bull Earthq Eng 9:809–823

Biondi G, Maugeri M (2005) Seismic response analysis of the Monte Po hill (Catania). In: Press W (ed) Seismic prevention of damage. A case study in a Mediterranean City (pp 177–195)

Bookhagen B, Burbank DW (2010) Toward a complete Himalayan hydrological budget: spatiotemporal distribution of snowmelt and rainfall and their impact on river discharge. J Geophys Res 115:F03019. https://doi.org/10.1029/2009JF001426

Cetin KO, Papadimitriou AG, Altun S, Pelekis P, Unutmaz B, Rovithis E, Akgun M, Klimis N, Askan A, Ziotopoulou K, Sezer A, Kincal C, Ilgac M, Can G, Cakir E, Soylemez B, Al-Suhaily A, Elsaid A, Zarzour M, Mylonakis G (2022) The role of site effects on elevated seismic demands and corollary structural damage during the October 30, 2020, M7.0 Samos Island (Aegean Sea) Earthquake. Bull Earthq Eng 20(14):7763–7792. https://doi.org/10.1007/S10518-021-01265-Z/FIGURES/30

Chang M, Tang C, Xiao CH et al (2016) Spatial distribution analysis of landslide triggered by the 2013–04–20 Lushan earthquake, China. Earthq Eng Eng Vib 15(1):163–171. https://doi.org/10.1007/s11803-016-0313-5

Chen X-L, Liu C-G, Yu L, Lin C-X (2014) Critical acceleration as a criterion in seismic landslide susceptibility assessment. Geomorphology 217:15–22. https://doi.org/10.1016/j.geomorph.2014.04.011

Chen XL, Liu CG, Wang MM (2019) A method for quick assessment of earthquake-triggered landslide hazards: a case study of the Mw6.1 2014 Ludian, China earthquake. Bull Eng Geol Environ 78(4):2449–2458

Chen Z, Huang D, Wang G (2023) A regional scale coseismic landslide analysis framework: integrating physics-based simulation with flexible sliding analysis. Eng Geol 315:107040. https://doi.org/10.1016/j.enggeo.2023.107040

Chevalier ML, Leloup PH, Replumaz A, Pan J, Metois M, Li H (2018) Temporally constant slip-rate along the Ganzi fault, NW Xianshuihe fault system, eastern Tibet. Geol Soc Am Bull 130(3/4):396–410. https://doi.org/10.1130/B31691.1

Chigira M, Wu X, Inokuchi T, Wang G (2010) Landslides induced by the 2008 Wenchuan earthquake, Sichuan, China. Geomorphology 118(3–4):225–238. https://doi.org/10.1016/j.geomorph.2010.01.003

Chousianitis K, Del Gaudio V, Kalogeras I, Ganas A (2014) Predictive model of arias intensity and newmark displacement for regional scale evaluation of earthquake-induced landslide hazard in Greece. Soil Dyn Earthq Eng 65:11–29. https://doi.org/10.1016/j.soildyn.2014.05.009

Cruden DM, Varnes DJ (1996) Landslide types and processes. Special Report-National Research Council, Transportation Research Board, p 247

Cui Y, Liu A, Xu C, Zheng J (2019) A modified Newmark method for calculating permanent displacement of seismic slope considering dynamic critical acceleration. Adv Civ Eng 2019:9782515, 10 p

Dai L, Fan X, Wang X et al (2023) Coseismic landslides triggered by the 2022 Luding Ms6.8 earthquake, China. Landslides 20:1277–1292. https://doi.org/10.1007/s10346-023-02061-3

di Lernia A, Buono C, Elia G (2023) Evaluation of seismic site effects in a real slope through 2D FE numerical analyses. 9th ECCOMAS Thematic Conference on Computational Methods in Structural Dynamics and Earthquake Engineering - COMPDYN2023, to be defined

European Space Agency, Sinergise (2021) Copernicus Global Digital Elevation Model. Distributed by OpenTopography. https://doi.org/10.5069/G9028PQB.Accessed:2023-04-13

Falcone G, Boldini D, Amorosi A (2018) Site response analysis of an urban area: a multi-dimensional and non-linear approach. Soil Dyn Earthq Eng 109:33–45

Gazetas G (1982) Vibrational characteristics of soil deposits with variable wave velocity. Int J Numer Anal Meth Geomech 6:1–20

Geli L, Bard P-Y, Jullien B (1988) The effect of topography on earthquake ground motion: a review and new results. Bull Seismol Soc Am 78(1):42–63. https://doi.org/10.1785/BSSA0780010042

Harp EL, Jibson RW (1996) Landslides triggered by the 1994 Northridge California earthquake. Bull Seismol Soc Am 86(1B):S319–S332. https://doi.org/10.1785/BSSA08601BS319

Hartmann J, Moosdorf N (2012) The new global lithological map database GLiM: a representation of rock properties at the Earth surface. Geochem Geophys Geosyst 13:Q12004. https://doi.org/10.1029/2012GC004370

Havenith H-B, Guerrier K, Schlögel R, Braun A, Ulysse S, Mreyen A-S, Victor K-H, Saint-Fleur N, Cauchi L, Boisson D, Prépetit C (2022) Earthquake-induced landslides in Haiti: analysis of seismotectonic and possible climatic influences. Nat Hazards Earth Syst Sci 22:3361–3384

Havenith H-B, Jongmans D, Faccioli E, Abdrakhmatov K, Bard P-Y (2002) Site effect analysis around the seismically induced Ananevo rockslide, Kyrgyzstan. Bull Seismol Soc Am 92(8):3190–3209

Havenith H-B, Torgoev I, Meleshko A, Alioshin Y, Torgoev A, Danneels G (2006) Landslides in the Mailuu-Suu Valley, Kyrgyzstan—hazards and impacts. Landslides 3(2):137–147. https://doi.org/10.1007/s10346-006-0035-2

He X, Xu C (2022) Spatial distribution and tectonic significance of the landslides triggered by the 2021 Ms6.4 Yangbi earthquake, Yunnan, China. Front Earth Sci. https://doi.org/10.3389/feart.2022.1030417

Huang S, Tang L, Hupy JP, Wang Y, Shao G (2021) A commentary review on the use of normalized difference vegetation index (NDVI) in the era of popular remote sensing. J For Res 32(1):1–6. https://doi.org/10.1007/s11676-020-01155-1

Jibson RW (1993) Predicting earthquake-induced landslide displacements using Newmark's sliding block analysis. Transport Res Rec 1411:9–17

Jibson RW (2007) Regression models for estimating coseismic landslide displacement. Eng Geol 91(2/4):209–218

Jibson RW (2011) Methods for assessing the stability of slopes during earthquakes-a retrospective. Eng Geol 122:43–50. https://doi.org/10.1016/j.enggeo.2010.09.017

Jibson RW, Keefer DK (1993) Analysis of the seismic origin of landslides: examples from the New Madrid seismic zone. Geol Soc Am Bull 105(4):521–536

Jibson RW, Harp EL, Michael JA (1998) A method for producing digital probabilistic seismic landslide hazard maps: an example from the Los Angeles California area. US Geol Surv Open-File Rep 98–113. 17 pp

Jibson RW, Harp EL, Michael JA (2000) A method for producing digital probabilistic seismic landslide hazard maps. Eng Geology 58(3–4):271–289. https://doi.org/10.1016/s0013-7952(00)00039-9

Jibson RW, Harp EL, Schulz W, Keefer DK (2004) Landslides triggered by the 2002 M-7.9 Denali Fault, Alaska, earthquake and the inferred nature of the strong shaking. Earthq Spectra 20:669–691

Jibson RW, Harp EL, Schulz W, Keefer DK (2006) Large rock avalanches triggered by the M 7.9 Denali Fault, Alaska, earthquake of 3 November 2002. Eng Geol 83(1):144–160. https://doi.org/10.1016/j.enggeo.2005.06.029

Jin KP, Yao LK, Cheng QG, Xing AG (2019) Seismic landslides hazard zoning based on the modified Newmark model: a case study from the Lushan earthquake, China. Nat Hazards 99:493–509. https://doi.org/10.1007/s11069-019-03754-6

Jin JL, Wang Y, Gao D, Yuan RM, Yang XY (2018) New evaluation models of Newmark displacement for Southwest China. Bull Seismol Soc Am 108(4):2221–2236. https://doi.org/10.1785/0120170349

Kawase H (2003) Site effects on strong ground motions. In: Lee WHK, Kanamori H (eds) International handbook of earthquake and engineering seismology Part B. Academic Press, London, pp 1013–1030. https://doi.org/10.1016/S0074-6142(03)80175-4

Keefer DK, Wilson RC, Bennett MJ, Harp EL (1989) Landslides in Central California: San Francisco and Central California July 20–29 1989.

Workshop on earthquake-induced landslides. American Geophysical Union, Washington D.C., pp 22–26. https://doi.org/10.1016/j.enggeo.2005.06.029

Khaple AK, Devagiri GM, Veerabhadraswamy N, Babu S, Mishra SB (2021) Chapter 6 - vegetation biomass and carbon stock assessment using geospatial approach. Forest Resources Resilience and Conflicts. p 77–91

Kramer S (1996) Geotechnical earthquake engineering. Prentice Hall, New Jersey

Kubo H, Kunugi T, Suzuki W et al (2020) Hybrid predictor for ground-motion intensity with machine learning and conventional ground motion prediction equation. Sci Rep 10:11871. https://doi.org/10.1038/s41598-020-68630-x

Kumar S, Gupta V, Kumar P, Sundriyal YP (2021) Coseismic landslide hazard assessment for the future scenario earthquakes in the Kumaun Himalaya, India. Bull Eng Geol Environ 80:5219–5235. https://doi.org/10.1007/s10064-021-02267-6

Li Y, Zhao D, Shan X, Gao Z, Huang X, Gong W (2022) Coseismic slip model of the 2022 Mw 6.7 Luding (Tibet) earthquake: preand post-earthquake interactions with surrounding major faults. Geophys Res Lett 49:e2022GL102043. https://doi.org/10.1029/2022GL102043

Liu X, Su P, Li Y, Xia Z, Ma S, Xu R, Lu Y, Li D, Lu H, Yuan R (2023) Spatial distribution of landslide shape induced by Luding Ms6.8 earthquake, Sichuan, China: case study of the Moxi Town. Landslides 20:1667–1678. https://doi.org/10.1007/s10346-023-02070-2

Lombardo L, Tanyas H (2022) From scenario-based seismic hazard to scenario-based landslide hazard: fast-forwarding to the future via statistical simulations. Stoch Env Res Risk Assess 36:2229–2242

Ma S, Xu C (2019) Assessment of co-seismic landslide hazard using the Newmark model and statistical analyses: a case study of the 2013 Lushan, China, Mw6.6 earthquake. Nat Hazards 96:389–412. https://doi.org/10.1007/s11069-018-3548-9

Maharjan S, Gnyawali KR, Tannant DD, Xu C, Lacroix P (2021) Rapid terrain assessment for earthquake-triggered landslide susceptibility with high-resolution DEM and critical acceleration. Front Earth Sci. https://doi.org/10.3389/feart.2021.689303

Miles SB, Ho CL (1999) Rigorous landslide hazard zonation using Newmark's method and stochastic ground motion simulation. Soil Dyn Earthq Eng. https://doi.org/10.1016/S0267-7261(98)00048-7

Moore ID, Grayson RB, Ladson AR (1991) Digital terrain modelling: a review of hydrological, geomorphological, and biological applications. Hydrol Process 5(1):3–30

Newmark NM (1965) Effects of earthquakes on dams and embankments. Géotechnique 15:139–160. https://doi.org/10.1680/geot.1965.15.2.139

Nsengiyumva JB, Luo G, Amanambu AC, Mind'je R, Habiyaremye G, Karamage F, Ochege FU, Mupenzi C (2019) Comparing probabilistic and statistical methods in landslide susceptibility modeling in Rwanda/Centre-Eastern Africa. Sci Total Environ 659(2019):1457–1472. https://doi.org/10.1016/j.scitotenv.2018.12.248

Prajisha CK, Achu AL, Joseph S (2023) Chapter 9 - Landslide susceptibility modeling using a generalized linear model in a tropical river basin of the Southern Western Ghats, India. Water, Land, and Forest Sustainability 1: 237–266

Shao X, Xu C, Wang P, Li L, He X, Chen Z, Huang Y, Xu X (2022) Two public inventories of landslides induced by the 10 June 2022 Maerkang Earthquake swarm, China and ancient landslides in the affected area. Nat Hazards Res. https://doi.org/10.1016/j.nhres.2022.09.001

Shinoda M, Miyata Y (2017) Regional landslide susceptibility following the Mid NIIGATA prefecture earthquake in 2004 with NEWMARK'S sliding block analysis. Landslides 14(6):1887–1899. https://doi.org/10.1007/s10346-017-0833-8

Shinohara Y, Kume T (2022) Changes in the factors contributing to the reduction of landslide fatalities between 1945 and 2019 in Japan. Sci Total Environ 827:154392. https://doi.org/10.1016/j.scitotenv.2022.15439

Taiebat M, Jeremić B, Dafalias YF, Kaynia K, Cheng Z (2010) Propagation of seismic waves through liquefied soils. Soil Dyn Earthq Eng 30(4):236–257. https://doi.org/10.1016/j.soildyn.2009.11.003

van den Bout B, Tang C, van Westen C, Jetten V (2022) Physically based modeling of co-seismic landslide, debris flow, and flood cascade. Nat Hazards Earth Syst Sci 22:3183–3209. https://doi.org/10.5194/nhess-22-3183-2022

Van Westen CJ, Van Asch WJ, Soeters R (2006) Landslide hazards and risk zonation: why is it still so difficult? Bull Eng Geol Environ 65:167–184. https://doi.org/10.1007/s10064-005-0023-0

Wang K-L, Lin M-L (2010) Development of shallow seismic landslide potential map based on Newmark's displacement: the case study of Chi-Chi earthquake, Taiwan. Environ Earth Sci 60(4):775–785. https://doi.org/10.1007/s12665-009-0215-1

Wang M, Shen ZK (2020) Present-day crustal deformation of continental China derived from GPS and its tectonic implications. J Geophys Res Solid Earth 125(2):e2019JB018774. https://doi.org/10.1029/2019JB018774

Wang G, Du C, Huang D, Jin F, Koo RCH, Kwan Julian SH (2018) Parametric models for 3D topographic amplification of ground motions considering subsurface soils. Soil Dyn Earthq Eng 115:41–54. https://doi.org/10.1016/j.soildyn.2018.07.018

Ward TJ, Li RM, Simons DB (1982) Mapping landslide hazards in forest watersheds. J Geotech Geoenviron Eng. https://doi.org/10.1061/AJGEB6.0001250

Wilson RC, Keefer DK (1983) Dynamic analysis of a slope failure from the 6 August 1979 Coyote Lake, California, earthquake. Bull Seismol Soc Am 73:863–877

Xi C, Hu X, Ma G et al (2022) Predictive model of regional coseismic landslides' permanent displacement considering uncertainty. Landslides 19:2513–2534. https://doi.org/10.1007/s10346-022-01918-3

Xiao Z, Xu C, Huang Y, He X, Shao X, Chen Z, Xie C, Li T, Xu X (2023) Analysis of spatial distribution of landslides triggered by the Ms 6.8 Luding earthquake in China on September 5, 2022. Geoenviron Disaster 10:3. https://doi.org/10.1186/s40677-023-00233-w

Xu C, Xu X, Shyu JBH (2015) Database and spatial distribution of landslides triggered by the Lushan, China Mw 6.6 earthquake of 20 April 2013. Geomorphology 248:77–92. https://doi.org/10.1016/j.geomorph.2015.07.002

Xue L, Li H-B, Brodsky EE, Xu Z-Q, Kano Y, Wang H, Mori JJ, Si J-L, Pei J-L, Zhang W, Yang G, Sun Z-M, Huang Y (2013) Continuous permeability measurements record healing inside the Wenchuan earthquake fault zone. Science. https://doi.org/10.1126/science.1237237

Yan B, Lin AM (2015) Systematic deflection and offset of the Yangtze River drainage system along the strike-slip Ganzi-YushuXianshuihe Fault Zone, Tibetan Plateau. J Geodynamics 87:13–25. https://doi.org/10.1016/j.jog.2015.03.002

Yang Z, Pang B, Dong W, Li D (2023) Spatial pattern and intensity mapping of coseismic landslides triggered by the 2022 Luding earthquake in China. Remote Sens 15:1323. https://doi.org/10.3390/rs15051323

Yin Y, Wang F, Sun P (2009) Landslide hazards triggered by the 2008 Wenchuan earthquake, Sichuan, China. Landslides 6:139–152. https://doi.org/10.1007/s10346-009-0148-5

Yu ZY, Yin N, Xiao P, Chen BX (2022) Co-seismic surface ruptures of the CE 1738 M 7.6 dangjiang earthquake along the NW continuation of the Xianshuihe fault zone and tectonic implications for the Central Tibetan Plateau. Front Earth Sci 10:810891. https://doi.org/10.3389/feart.2022.810891

Yuan R, Deng Q, Cunningham D, Han Z, Zhang D, Zhang B (2016) Newmark displacement model for landslides induced by the 2013 Ms 7.0 Lushan earthquake, China. Front Earth Sci 10(4):740–750. https://doi.org/10.1007/s11707-015-0547-y

Zang M, Qi S, Zou Y, Sheng Z, Zamora BS (2020) An improved method of Newmark analysis for mapping hazards of coseismic landslides. Nat Hazards Earth Syst Sci 20:713–726. https://doi.org/10.5194/nhess-20-713-2020

Zevenbergen LW, Thorne CR (1987) Quantitative analysis of land surface topography. Earth Surf Proc Land 12(1):47–56

Zêzere JL, Pereira S, Melo R, Oliveira S, Garcia RAC (2017) Mapping landslide susceptibility using data-driven methods. Sci Total Environ. https://doi.org/10.1016/j.scitotenv.2017.02.188

Danny Love Wamba Djukem · Xuanmei Fan (✉) · Xin Wang · Lanxin Dai · Chengyong Fang · Xinxin Zhang · Qiang Xu
State Key Laboratory of Geohazard Prevention and Geoenvironment Protection, Chengdu University of Technology, Chengdu 610059, China

Xuanmei Fan
Email: 18202308@qq.com

Anika Braun
Department of Engineering Geology, Institute of Applied Geosciences, Technische Universität Berlin, Ernst-Reuter-Platz 1, BH 3-1, Berlin 10587, Germany

Marie-Luce Chevalier
Key Laboratory of Continental Dynamics of Ministry of Natural Resources, Institute of Geology, Chinese Academy of Geological Sciences, Beijing 100037, China

Tolga Gorum
Istanbul Technical University, Eurasia Institute of Earth Sciences, 34469 Sarıyer Maslak, Istanbul, Turkey

Hans-Balder Havenith
Geology Department - B18, Georisk and Environment, Liege University, Sart Tilman, Liege B-4000, Belgium

Hans-Balder Havenith
Email: hb.havenith@uliege.be